Polarity and direction dependence of energetic cross-frontal eddy transport in the Southern Ocean's Pacific sector

Huimin WANG[1], Lingqiao CHENG[1,5*], Erik BEHRENS[2], Zhuang CHEN[1,4,5], Jennifer DEVINE[3], Guoping ZHU[4,5,6,7]

[1]*College of Oceanography and Ecological Science, Shanghai Ocean University, Shanghai, China*
[2]*Earth Sciences New Zealand, Wellington, New Zealand*
[3]*Earth Sciences New Zealand, Nelson, New Zealand*
[4]*College of Marine Living Resource Sciences and Management, Shanghai Ocean University, Shanghai, China*
[5]*Center for Polar Research, Shanghai Ocean University, Shanghai, China*
[6]*Polar Marine Ecosystem Group, The Key Laboratory of Sustainable Exploitation of Oceanic Fisheries Resources, Ministry of Education, Shanghai, China*
[7]*International Research Center for Marine Biosciences at Shanghai Ocean University, Ministry of Science and Technology, China*

* **Correspondence:** Lingqiao Cheng (lqcheng@shou.edu.cn)

Abstract:

~~Cross-frontal m~~Mesoscale eddies play a critical role in mediating~~e~~ meridional ~~heat and mass~~ transport across the Antarctic Circumpolar Current (ACC)~~, fronts.~~ y~~Y~~et the dynamics of cross-frontal eddies (CFEs) and their energy exchanges with frontal jets~~spatiotemporal characteristics and dynamical impacts in the Southern Ocean's Pacific sector~~ remain inadequately quantified. This study presents a systematic analysis of CFE characteristics, kinetic energy evolution, and thermohaline transport effects in the Pacific sector of the Southern Ocean, u~~U~~tilizing 23 years (2000–2022) of satellite altimetry and Argo float data. Our results~~, we~~ reveal a fundamental~~, for the first time, a pronounced~~ polarity- and direction-dependent asymmetry in~~ce in cross-frontal eddy (~~CFE~~) abundance~~ dynamics.~~, energetics, and interactions with jets.~~ Equatorward-propagating cyclonic eddies (CEs) dominate CFE activity, followed by poleward-moving anticyclonic eddies (AEs).~~ (36% of total)~~ These dominant~~,~~ CFE types exhibit~~ing~~ superior energetic characteristics, including significantly higher~~higher~~ eddy kinetic energy (*EKE*~~, in terms of total *EKE* in eddy interiors, EKE_T~~)~~ levels , longer propagation distances,~~ and stronger nonlinearity compared to their~~than other~~ counterparts~~types~~. Complete CFEs experience polarity- and direction-selective energy gains during frontal crossing, with equatorward CEs and poleward AEs extracting energy from eastward frontal jets, while their counterparts lose energy. This energization mechanism has intensified over the past two decades, with both polarity CFEs showing substantial *EKE* increases that substantially exceed previous basin-scale estimates. Hydrographic analysis demonstrates that CEs and AEs transport distinct water masses across frontal boundaries, creating sharp~~, followed by poleward-moving anticyclonic eddies (AEs, 2830%). These two dominant directional groups primarily drive the significant increase in the overall CFEs' EKE_T: CEs at (2.27 ± 1.45)(1.98 ± 1.53) × 10^6 $m^4 s^{-2} yr^{-1}$ (excluding the anomalously low 2017 value) and AEs at (12.58 27 ± 00.7494) × 10^6 $m^4 s^{-2} yr^{-1}$. Specifically, complete CFEs (experience pre-crossing, crossing, and post-crossing phases) are responsible for these trends, distinct from non-CFEs, partial or transient CFEs, which show no trend. During frontal crossing, EKE_T enhances in equatorward CEs and poleward AEs but diminishes in poleward CEs and equatorward AEs, explaining the two former types' capacity for long-distance propagation and energetic behaviors. The intensified CEs carry cold, fresh southern waters equatorward, while AEs transport warm, salty northern waters poleward. These cross-frontal exchanges mitigate~~ thermohaline contrasts within~~gradients between~~ interfrontal zones. Our findings establish CFEs as crucial regulators that buffer wind- and warming- induced baroclinicity increases through compensatory heat transport, thereby maintaining the Southern Ocean's thermal equilibrium and modulating the ACC's response to external forcing in a changing climate. ~~while enhancing local mesoscale available potential energy. We conclude~~

~~that CFEs serve dual climatic roles, in mediating meridional energy transport while dynamically stabilizing the ACC against strengthening winds.~~

Keywords: Cross-frontal eddies; Eddy kinetic energy; Meridional ~~Spatiotemporal characteristics~~transport; ~~Energy transfer;~~ Antarctic Circumpolar Current; the Pacific sector of the Southern Ocean

1 Introduction

Mesoscale eddies are ubiquitous in the Southern Ocean (SO), play a vital role in the zonal and meridional transport of quantities including heat and momentum across the Antarctic Circumpolar Current (ACC), and also influence the uptake of heat and carbon dioxide from the atmosphere (Moreau et al., 2017; Patel et al., 2019; Sallée et al., 2008; Sokolov and Rintoul, 2007) and the transport and connectivity of marine species (e.g., Duan et al., ~~2021~~2020; Zhu et al., 2025). The ACC comprises multiple zonal fronts, where oceanic jets exit. Here, a front refers to a boundary between distinct water masses, characterized by strong horizontal density gradients, while a jet denotes the narrow, swift current that flows along the axis of such a front. Together, they form the dynamic core of the ACC.~~The ACC comprises multiple zonal fronts, where oceanic jets exit.~~ At these fronts, mesoscale activity is enhanced, with higher eddy kinetic energy (*EKE*) and more frequent eddy generation and dissipation (Barthel et al., 2017; Gille, ~~2012~~1994; Hughes, ~~2012~~1995; Hughes and Ash, 2001; Morrow et al., 1994; Sokolov and Rintoul, 2002). In turn, eddies impact the fronts' structure, intensity, and location. For instance, eddies may accelerate the jets, and cyclonic (anticyclonic) eddies cause the equatorward (poleward) deviation of frontal meanders in some cases (Chapman et al., 2020; Duan et al., 2016; Frenger et al., 2015; Sprintall, 2003). These interactions between mesoscale eddies and oceanic fronts can shape local thermohaline structures, exert profound influences on large-scale circulation and vertical flux processes. They also have tremendous implications for the redistribution and survival of marine species and the stability of the climate system.

In the SO, the transition from the warm subtropical waters to the cold Antarctic waters is not smooth but concentrated along a series of fronts (Orsi et al., 1995; Belkin and Gordon, 1996) ~~(Deacon, 1937)~~, often corresponding to the locations of narrow, high-speed currents known as "jets" (Sokolov and Rintoul, 2002, 2007). These fronts delineate the boundaries of distinct water masses, each with unique environmental characteristics (Orsi et al., 1995). The existence of fronts hinders meridional exchanges of heat and tracers (Chapman and Sallée, 2017; Naveira Garabato et al., 2011; Thompson and Sallée, 2012). At the same time, eddies enable cross-frontal transport and serve as primary carriers for meridional water mass properties, including heat (De Szoeke and Levine, 1981; Foppert et al., 2017). ~~Practically,~~ Cross-frontal eddies (CFEs) must overcome intense geostrophic shear to achieve material transport and render their dynamical contributions to meridional transport, which is significantly more pronounced compared to other eddy types (Thompson and Sallée, 2012).

Eddies' capability of trapping materials and achieving long-distance cross-frontal transport helps in mitigating sharp meridional hydrographic gradients, facilitating new water formation and carbon transport, and also enhancing subsurface temperature extremes in the SO. Holte et al. (2013) presented that cross-frontal exchanges by eddies can penetrate strong potential vorticity gradients associated with the Subantarctic Front (SAF) and facilitate the downstream evolution of Subantarctic Mode Water by transporting cold, low-salinity water across the ACC from the Polar Front Zone (Holte et al., 2013). In a study of a cold eddy in the southwest Indian Ocean, Swart et al. (2008) found that the eddy displaced temperature and salinity anomalies by 1.5° towards lower latitudes. This single eddy contributed 2.5% of the annual northward flux of Antarctic Surface Water in the southwest Indian sector (Swart et al., 2008). In addition, eddies induce carbon transport across the ACC, which alters the carbon properties and budget of the Subantarctic Zone waters (Moreau et al., 2017). Patel et al. (2019) proposed that about 21% of the heat transported across the SAF to the Subantarctic Zone south of Tasmania is achieved by cyclonic eddies. He et al. (2023) demonstrated that nearly half of the subsurface temperature extremes in the Southern Ocean occur within eddies, with cross-frontal eddies (CFEs) generating extremely high-temperature events on the cold side of the ACC and extremely low-temperature events on the warm side. These extremes eventually impact marine organisms and ecosystems. ~~He et al. (2023) demonstrated that nearly half of the observed subsurface temperature extremes in the SO occur within eddies; CFEs act as a source of extremely high-temperature events on the cold side of the ACC and extremely low-temperature events on the warm side; These temperature extremes eventually impact marine organisms and ecosystems.~~ For instance, *Electrona carlsbergi* in the high-latitude

Antarctic region may be transported across the fronts from the Argentine Basin by the poleward eddy activity (Saunders et al., 2017; Zhu et al., 2025).

Eddies in the SO can moderate the ACC’s response to surface wind forcing changes, namely the “eddy saturation” hypothesis (Hallberg and Gnanadesikan, 2001, 2006; Straub, 1993). Reanalysis of data since 1972 show an increasing trend in wind stress (associated with a positive trend of Southern Annular Mode) over the Pacific sector that dominates the basin-wide wind stress variability, driving enhanced eddy activity responses in this sector, with *EKE* intensifying at a rate of 14.9 ± 4.1 m^4 s^{-2} per decade (Duan et al., 2016; Hogg et al., 2015; Menna et al., 2020; Morrow et al., 2010). Recent work by Zhang et al. (2021) demonstrates that *EKE* intensification is not spatially homogeneous in the SO but concentrated south of New Zealand and downstream of the Campbell Plateau in the Pacific sector. This localized enhancement likely stems from the release of available potential energy stored in tilted isopycnals, thus acting to~~ereby~~ ~~counteracting~~moderate~~mitigating~~ the eastward flow in the ACC, which has significantly intensified between 48°S and 58°S mainly due to buoyancy forcing (Shi et al., 2021). Mesoscale energy gain from mean flows is achieved through baroclinic (primary) and barotropic (secondary) pathways (Fu et al., 2023). Regarding topographic effects, previous studies have established that interactions between ACC and seafloor topography intensify oceanic eddy mixing by enhancing downstream baroclinic shear. This process enhances eddy generation and increases *EKE* downstream of major topographic features (Frenger et al., 2015; Morrow et al., 1992; Park et al., 1993; Thompson and Sallée, 2012). Consequently, ACC frontal jets with strong geostrophic characteristics experience mesoscale eddy modulation near prominent topographies (Kim and Orsi, 2014; Thompson et al., 2010).

Despite extensive research on basin-scale *EKE* modulations and case studies of CFE transport, and the well-established asymmetric eddy distribution on both sides of the ocean fronts, fundamental questions remain regarding how eddy-jet interactions vary based on eddy characteristics and directional approach in the SO. Specifically, it is essential to understand: (1) the polarity and direction preferences of CFEs during frontal crossing; (2) the magnitude and pattern of kinetic energy change within eddies following frontal crossing; (3) the resultant hydrographic property redistribution achieved by CFEs in the interfrontal zones. Motivated by these research gaps, we conducted a systematic assessment of cross-frontal mesoscale eddies in the Pacific sector to elucidate their role in regional ocean dynamics and hydrographic redistribution. Utilizing 23 years (2000–2022) of satellite altimetry data, we characterize the spatiotemporal variability, *EKE* patterns, and eddy-jet interactions of CFEs in the Pacific sector. We complement these analyses with Argo (Array for Real-time Geostrophic Oceanography) float profiles to quantify normalized hydrographic differences between cyclonic and anticyclonic eddies within the interfrontal zones. These approaches aim to improve our understanding of the dynamic characteristics of CFEs and their role in mediating meridional transport across the ACC in this sector.

2 Data and methods

2.1 Data

This study focuses on the SO's Pacific sector ~~between~~in the range of 150°E–110°W,~~ and~~ 35°S–80°S. Prominent topographic features within this region include the Campbell Plateau, Pacific-Antarctic Ridge, Eltanin Fracture Zone, and Udintsev Fracture Zone (Figure 1). We utilized the gridded satellite altimeter data for eddy detection and tracking. This dataset is merged from multiple satellites and provided by the Copernicus Marine Service as the CMEMS all-satellite L4 SLA product, ~~the Level-4 product~~ SEA LEVEL_GLO_PHY_L4_~~NRT~~MY_008_047~~6~~ (Copernicus Marine Service, 2024~~Version 1.0, released 28 May~~

~~2025; Pujol and Grassi, 2025~~). The data were accessed/downloaded on 18 December 2025 from the Copernicus Marine Service Information (DOI: https://doi.org/10.48670/moi-00148). ~~It includes daily Sea Level Anomaly (SLA) and sea surface geostrophic velocity anomalies (u', v') data from 2000 to 2022, with a spatial resolution of 0.125°×0.125°. The data were accessed via https://doi.org/10.48670/moi-00148 on 18 December 2025. This dataset is merged from multiple satellites and provided by the Copernicus Marine Service (Global Ocean Gridded L4 Sea Surface Heights And Derived Variables at https://marine.copernicus.eu/).~~ It includes daily Sea Level Anomaly (*SLA*) and sea surface geostrophic velocity anomalies (*u'*, *v'*) data during 2000~~ and ~~–2022 with a spatial resolution of 0.125°×0.125°. The *SLA* represents the sea surface height anomaly relative to the mean sea surface from 1993 to 2012. The corresponding geostrophic velocity anomalies (*u'*, *v'*)~~(u′, v′)~~ are~~ provided within the same dataset,~~ derived from *SLA* based on the geostrophic balance~~. For detailed processing algorithms, users may refer to the product documentation~~ (Pujol and Grassi, 2025).~~The *SLA* is the sea surface height anomaly relative to the mean sea surface from 1993 to 2012. *u'*, *v'* were calculated from *SLA* based on the geostrophic relation:~~

~~$u'=-\frac{g}{f}\frac{\partial SLA}{\partial y}, v'=\frac{g}{f}\frac{\partial SLA}{\partial x}$, (1)~~

~~where *g* is the acceleration of gravity (m s^{-2}), *f* is the Coriolis parameter (s^{-1}), *x* and *y* are the zonal and meridional distances (m), respectively.~~

The geographical positions of the ACC's fronts and boundaries used in this study are from the synthesis of Park et al. (2019). This dataset provides the most updated mapping of the ACC frontal system and its associated boundaries, derived from satellite altimetry and independently validated against extensive subsurface observations, including Argo float profiles (2001–2017) and dedicated CTD surveys (2016–2017). As shown in Figure 1, the dataset defines five major streamlines from north to south: the Northern Boundary (NB), the Subantarctic Front (SAF), the Polar Front (PF), the Southern ACC Front (SACCF), and the Southern Boundary (SB). Specifically, the NB represents the northern dynamical limit of the ACC and coincides with the northern expression of the Subantarctic Front system (SAF-N) in this region. The SAF, PF, and SACCF correspond to the core frontal jets.

~~The geographical positions of the ACC's frontsal jets and boundaries used in this study are from the synthesis of Park et al. (2019). This dataset provides the most updated mapping of the ACC frontal system and its associated boundaries, derived from satellite altimetry and independently validated against extensive subsurface observations, including Argo float profiles (2001–2017) and dedicated CTD surveys (2016–2017).~~

~~As shown in Figure 1, the dataset defines five major streamlines from north to south: the Northern Boundary (NB), the Subantarctic Front (SAF), the Polar Front (PF), the Southern ACC Front (SACCF), and the Southern Boundary (SB). Specifically, the NB streamline represents the northern dynamical limit of the ACC in their analysis and coincides with the northern expression of the Subantarctic Front system (SAF-N) in this region, while the SAF, PF, and SACCF correspond to the core frontal jets.~~

~~The frontal data used in this study were sourced from Park et al. (2019). In their frontal identification process, the climatological positions of the ACC fronts were determined using the CNES-CLS18 mean dynamic topography (Mulet et al., 2012) derived from satellite altimetry. Then, subsurface temperature data (2001–2017) from Argo floats were employed to validate the satellite-derived frontal positions. In addition, high-quality hydrographic data from two CTD (Conductivity-Temperature-Depth) surveys conducted in 2016 and 2017 further verified the ACC frontal structures. By integrating these datasets, Park et al. (2019) produced the most updated mapping of the ACC fronts. As shown in Figure 1, from north to south, the key fronts include the northern boundary of ACC (NB), the Subantarctic Front (SAF), the Polar Front (PF), the Southern Antarctic Circumpolar Current Front (SACCF), and the southern boundary of the ACC (SB).~~

Furthermore,~~ we utilized~~ a total of ~~1,165~~1094 quality-controlled Argo profiles (0–2000 m; https://argo.ucsd.edu/data/~~http://www.argo.net~~) located within ~~observed in~~ detected eddies were utilized to analyze the internal thermohaline structure of cyclonic (CEs) and anticyclonic eddies (AEs)~~.~~ T~~to~~~~They were used to normalize t~~he~~ internal~~ potential temperature (θ) and salinity (S) within each eddy were normalized radially by binning profiles according to their relative ~~properties in cyclonic eddies (CEs) and anticyclonic eddies (AEs) in the interfrontal zones. The~~ normalized ~~normalized potential temperature (θ) and salinity (S) in the radius direction were derived by matching Argo profiles to eddies based on the ratio of their~~ distance from the eddy center (normalized by ~~to~~ the eddy radius, ~~(~~R), at an~~ with an~~~~. The~~ average interval~~s~~ of~~were~~ 0.03~~06~~R~~ for CEs and 0.004R for AEs, respectively, based on sample density~~. Owing~~Due~~ to limited spatial~~Argo float~~ coverage, profiles from the SB-SACCF zone and areas south of the SB were excluded. Consequently, ~~temporal variability (e.g., interannual and seasonal) was not considered in this normalizing process, and the SB-SACCF region and those south of SB were omitted. This~~the analysis focused~~s only~~ on the northern inter-frontal zones of SAF-NB, PF-SAF, and SACCF-PF, which contained~~where~~ 400~~400~~, 150~~ 150~~, and 252~~252 Argo~~ profiles~~ in eddy interiors were detected~~, respectively. Furthermore, temporal variability (e.g., interannual and seasonal) was not considered in this composite analysis due to the uneven distribution of profiles over time.

~~Additionally, the material coherence and cross-frontal transport capability of the eddies tracked by our algorithm were validated using independent in situ Lagrangian evidence. This validation leveraged serendipitous instances where long-lived eddies entrapped Argo profiling floats for extended periods (up to several months). The trajectories of these floats, coupled with the persistent thermohaline anomalies recorded throughout their entrapment, directly confirm that the algorithm identifies physically coherent vortices capable of transporting water masses across frontal boundaries.~~

2.2 Eddy detection, tracking and CFE categorization

We combined the Okubo-Weiss (OW) parameter method with the outermost closed contour of *SLA* to detect eddies. As a widely used eddy detection method, the OW parameter method was developed based on flow field deformation by high vorticity or high strain (Okubo, 1970; Weiss, 1991). The OW parameter is defined as:

$$W = s_n^2 + s_s^2 - \omega^2, \qquad (2)$$

where $s_n = \frac{\partial u'}{\partial x} - \frac{\partial v'}{\partial y}$ and $s_s = \frac{\partial v'}{\partial x} + \frac{\partial u'}{\partial y}$ are the normal and shear components of strain, respectively, and $\omega = \frac{\partial v'}{\partial x} - \frac{\partial u'}{\partial y}$ is the relative vorticity of the flow. The sign of W determines a region to be strain-dominated ($W > 0$) or vorticity-dominated ($W < 0$). Eddies are highly vorticity-dominated circulations, thus corresponding to coherent negative-W areas (for both CEs and AEs), and the negative W must be larger than that for the background field (Henson and Thomas, 2008).

To identify physically consistent eddy boundaries, we adopt the hybrid geometric–physical approach validated by Saraceno and Provost (2012), which avoids common biases associated with fixed W thresholds. ~~In this study, we identify eddies as contiguous regions where $W < -0.2\sigma_W$. Here, σ_W is the spatial standard deviation of W calculated for each daily snapshot over the entire study domain (e.g., Henson and Thomas, 2008; Isern-Fontanet et al., 2006). The final threshold value uses the temporal mean of these daily σ_W values over the entire study period. This threshold, while empirical and without a universal physical basis (Pasquero et al., 2001), has been widely adopted in mesoscale eddy detection. Critically, it has been specifically applied and validated for the Southern Ocean using the same altimetry product by Frenger et al. (2015), whose study provides a key regional justification for our parameter choice.~~ A~~A~~ threshold of W $<$~~=~~ -0.2 σ_w is ~~was~~ often used ~~chosen~~ to delineate eddy boundaries~~identify the outer boundary of an eddy,~~, with σ_w being the standard deviation of W over the entire region (e.g., Henson and Thomas, 2008; Isern-Fontanet et al., 2006; Frenger et al., 2015). However, this~~e threshold-based~~

method can underestimate ~~used on the *W* value may cause an underestimation of the~~ eddy area in ~~some specific~~certain regions (Matsuoka et al., 2016) and misidentify meanders as eddies in energetic frontal zones (Saraceno and Provost, 2012). Our approach proceeds as follows: after detecting the eddy center using the OW-based method, we identify~~y~~ the outermost closed *SLA* contour that encloses this point. This contour defines the eddy boundary, and the center was~~is~~ then recalculated as its geometric centroid. Eddy radius was~~is~~ computed as the radius of a circle of equivalent area, and eddy amplitude is the absolute *SLA* difference between the center and along the contour.~~Thus, we defined the outermost closed contour of *SLA* as the eddy boundary, with its radius equated to that of a concentric circle whose area matches the closed contour area. SLA data were obtained from the Copernicus Marine Environment Monitoring Service (CMEMS) Level-4 gridded product SEALEVEL_GLO_PHY_L4_NRT_008_046 [Pujol and Grassi, 2025; CMEMS, 2025]. This dataset provides daily SLA fields with a native horizontal resolution of 0.125° (approximately 14 km at the equator), which is considered sufficient to resolve mesoscale ocean eddies for the purposes of this study~~~~Thus, we defined the outermost closed contour of SLA as the eddy boundary, with its radius equated to that of a concentric circle whose area matches the closed contour area. The SLA data have a native spatial resolution of 0.125°×0.125°, which is adequate for resolving the mesoscale eddies targeted in this study.~~

For eddy tracking, the algorithm identifies eddies at time t+1 that meet the following criteria relative to time t: (1) minimal centroid distance, (2) identical polarity (i.e., rotation direction), and (3) the minimum radius variation. If no eddy at t+1 satisfies these proximity thresholds for a given eddy at t, the eddy is considered dissipated. Conversely, if an eddy detected at t+1 does not match any eddy at t, it is classified as a newly generated eddy.

To ensure ~~the~~ statistical robustness~~s of our analysis~~, our ~~we~~ analysis focused exclusively ~~focused~~ on significant mesoscale eddies, which were defined as well-resolved, energetic eddies with sufficient temporal coherence. Eddies meeting all of the following criteria were retained as the core dataset for subsequent analyses: (1)~~that are well-resolved by the data. We applied a set of selection criteria requiring eddies to~~ radius > 30 km; (2) amplitude > 5 cm; and (3)~~have a~~ lifespan >~~exceeding~~ 14 days. ~~(to ensure temporal coherence given the daily data resolution), an amplitude greater than 5 cm (to select energetically strong signals), and a radius larger than 30 km (to guarantee the eddy structure is sufficiently larger than the ~14 km native grid scale). Eddies meeting all these conditions were classified as significant eddies and constituted the core dataset for all subsequent analyses.~~~~Based on eddy identification and tracking results, this study focuses on eddies with lifespans exceeding 14 days, amplitudes greater than 5 cm, and radii greater than 30 km.~~

The *EKE* was computed from geostrophic velocity anomalies using the equation $EKE=$~~1/2~~$(u'^2+v'^2)$/2. In this study, except for Figure 1, all analyses of *EKE* variation during cross-frontal processes were based on the total *EKE* within each eddy interior (EKE_T) for better tracking *EKE* changes in specific eddies, calculated as $EKE_T = \sum_{i=1}^{N} EKE_i \cdot ds$, where EKE_i is the *EKE* for grid *i*, *N* is the grid amount within an eddy, and *ds* is the grid area. The eddy nonlinearity parameter (β) was computed based on $\beta = U/C$, where *U* is the maximum circum-average geostrophic velocity within the eddy, and *C* represents the eddy's transporting speed (Chelton et al., 2011). The eddy is nonlinear when $\beta > 1$, indicating the presence of trapped fluid parcels advected with the eddy movement.

While climatological fronts define the ACC's mean structure (Park et al., 2019), their positions exhibit meridional variability influenced by both bathymetry and eddy activity (Kim and Orsi, 2014; Thompson et al., 2010~~);~~). Fronts stabilize over major bathymetric features (e.g., the Pacific-Antarctic Ridge) but show~~show~~ maximum variability in flat basins.~~,~~ Due to eddy-mean flow interaction processes,~~with widened~~ frontal zones become greater ~~developing~~ downstream of topographic obstacles like the Campbell Plateau. Based on the observed frontal variability in the Pacific sector, the maximum total meridional frontal drift during 1993–2010 is approximately 80 km southward (at 150°E), and annual cycle amplitude is < 40 km (Kim and Orsi, 2014). To account for ~~topographically induced~~these frontal displacements, we first defined a baseline frontal zone~~s~~ as a ~~strap~~ ±15 km strap in the normal direction from each~~expanded in the normal directions from each~~ climatological front.~~,~~ Then,~~This width is consistent with the magnitude of observed frontal oscillations in the SOSouthern Ocean and is particularly justified in our study region (the Pacific sector) where seasonal frontal migration is minimal consistent with observed SO frontal oscillation area (< 10 km, Kim and Orsi, 2014).~~

t~~T~~o objectively ~~unambiguously~~ identify~~determine~~ eddy-front interactions, we applied a ~~when an eddy interacts with a frontal zone, we applied the following~~ geometric criterion ~~based on the eddy''s instantaneous identified radius R~~: an eddy was considered interacting when its boundary contacted the frontal zone. Since all analyzed eddies have a radius (*R*) > 30 km, this criterion effectively creates a dynamic interaction zone with a minimum half-width of 45 km (15 km + 30 km), ~~to have entered (exited) the frontal zone once its boundarywhen any part of its circular contour (defined by its center and radius R) first first touched (lastfinally completely detached from) the frontal zone boundary. This effectively expands the frontal interaction zone by ±R on each side, with R varying per eddy~~which comfortably exceeds the observed ranges of frontal variability. To further ensure robustness, we conducted a sensitivity analysis by expanding the frontal zones to a ±25 km strap (see Supplementary Materials), which confirmed that all key findings are insensitive to the exact zone definition.

The ~~, e~~Eddy-front interaction was then divided ~~Thereby, we classified CFE dynamics~~ into three sequential phases: pre-cross-frontal ~~(approaching the frontal zone)~~, cross-frontal ~~(within the frontal zone)~~, and post-cross-frontal~~ (exiting the frontal zone)~~. ~~For statistical analysis,~~ CFEs were further categorized into four types: (1) Front-generated eddies, generated within the dynamic interaction zone and subsequently propagating away, (2) Front-dissipated eddies, propagating into the dynamic interaction zone and dissipated there, (3) Transient frontal eddies, ~~(~~both generated and dissipated within the same interaction~~frontal~~ zone~~s)~~, and (4) Complete CFEs, ~~(~~undergoing all three phases (pre-, cross-, and post-frontal~~three phases~~) relative to the dynamic interaction zone. Both types (1~~a~~) and (1~~b~~) eddies ~~Accordingly, front-generated eddies propagating away (type 1−3) and eddies propagating into the frontal zones and dissipating there (type 2−3)~~ were collectively classified~~ identified~~ as partial CFEs. Hereafter, all frontal zones refer to dynamic interaction zones. Notably, according to the definition, the partial frontal crossing eddies of Type 1 include rings pinched off from the meandering structures of a front.

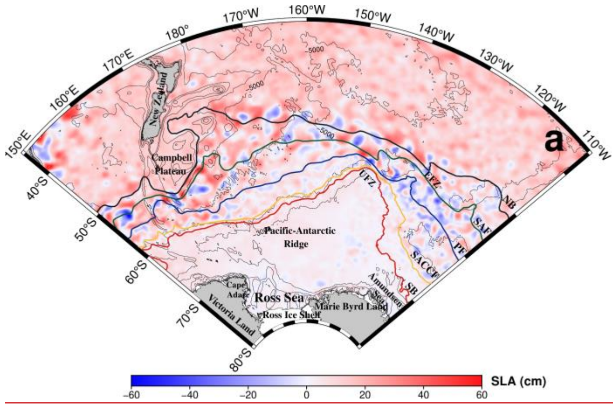

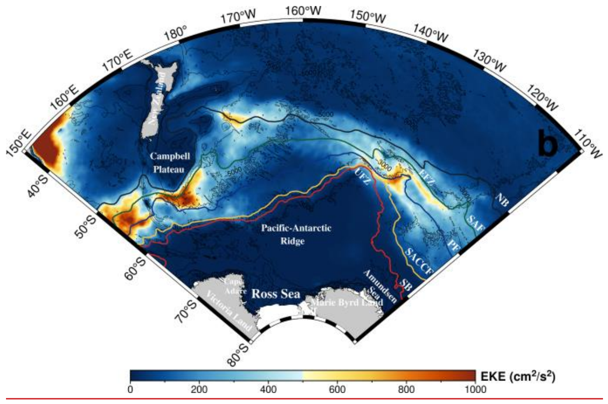

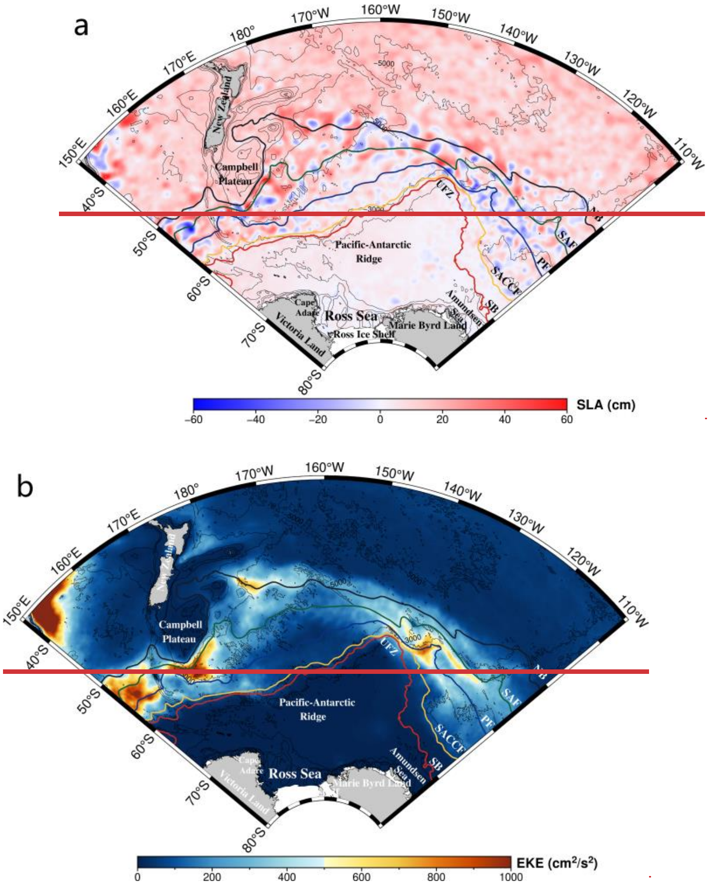

Figure 1. Study region. (a) Sea Level Anomaly (*SLA*) distribution on January 20th, 2022. (b) Spatial distribution of mean eddy kinetic energy (*EKE*) during 2000–2022. Thick colored lines from north to south represent the northern boundary of ACC (NB), the Subantarctic Front (SAF), the Polar Front (PF), the Southern Antarctic Circumpolar Current Front (SACCF) and the southern boundary of ACC (SB; Park et al., 2019). Significant seafloor topographies have been labeled, with UFZ denoting the Udintsev Fracture Zone. The abbreviation EFZ denotes the Eltanin Fracture Zone.

3 Results

3.1 Analysis of CFE characteristics

CFE transport is active across all major ACC frontal zones~~ and its northern boundary~~ in the Pacific sector (Figure 2)~~CFE transport is active at all ACC fronts in the Pacific sector (Figure 2)~~. At each front, e~~E~~quatorward-moving CFEs consistently outnumber poleward-moving eddies~~ at each front~~ (Figure 2b). CEs dominate equatorward CFEs, with CEs outnumbering AEs by a factor of ≥1.5, while AEs prevail in poleward CFE motions. The resulting hierarchy of CFE prevalence is as follows: equatorward CEs are the most frequent (36% of total CFEs), followed by poleward AEs (30%) and equatorward AEs (18%), with poleward CEs (16%) being the least frequent. Among the different frontal zones~~ and the northern boundaryAmong different fronts~~, the SAF hosts the most eddy occurrences (30% of total CFEs), followed by the PF (27%), reflecting intense eddy-mean flow interactions around these two fronts. The northernmost ~~boundary (~~NB (~~,~~23% of total CFEs)~~The NB (23% of total CFEs)~~ and the SACCF (16%) exhibit comparable and moderate CFE levels, while the southernmost SB (7%) displays the lowest CFE exchanges.

The frontal system exhibits strong meandering patterns due to topographic steering, accompanied by spatially heterogeneous CFE distributions. CFE occurrence peaks downstream of prominent topographic features, particularly near the Campbell Plateau (150°E–180°E; 41% of total CFEs) and downstream of the Udintsev Fracture Zone (125°W–160°W; 38%), where multiple fronts converge (Figure 2a). Eddies may cross multiple fronts sequentially at these frontal convergent regions. The majority of eddies cross a single front (Figure 2c). Double-frontal crossings (total 411) occur preferentially at southern fronts (SACCF/SB; > 50% of cases; Figure 2d). Triple-frontal crossings are rare and primarily limited to the PF/SACCF/ SB system (Figure 2e), and no instances of quadruple-frontal crossings were observed.

Consistent with the ACC dynamics, over 70% of ~~both~~ cross-frontal CEs and AEs ~~predominantly~~ propagate eastward (~~> 70% of cases;~~ Figure 3), a notable contrast~~ing~~ to the~~with~~ typical westward propagation of mesoscale eddies driven by Rossby waves~~-driven westward-propagating mesoscale eddies~~ in other ocean basins (Frenger et al., 2015). Short-distance movements (< 2°) are more frequent for AEs at each front. In contrast, CEs dominate l~~L~~ong-distance propagation~~ing eddies~~, particularly ~~are concentrated~~ at~~near~~ the SAF and PF~~, with CEs being the main contributors.~~ The majority of CEs propagate northward (over 64% of all CEs)~~, with maximum displacements reaching approximately 8° latitude~~, while over 54% of~~.~~ AEs are ~~more inclined to~~oriented~~ move~~ southward~~ (over 54% of all AEs), with southward displacements confined within 6° latitude~~. The greater energetic content of ~~Percentages in Figure 3 show that short-distance movements (within 2°) are more frequent for AEs at each front. The~~ CEs, as indicated by their~~,~~ dominance in long-distance transport, aligns with their role as primary agents of meridional exchange.~~ indicates their greater energetics compared to AEs.~~ These patterns highlight how ACC-steered eddy motions facilitate distinct ~~meridional exchange~~transport pathways, with CEs~~ playing a~~ disproportionately driving ~~role in~~ long-distance exchanges~~transport~~, particularly at~~ the~~ major fronts~~al jets~~ such as the SAF and PF.

~~–~~Most CFEs (99%) exhibit nonlinear characteristics~~, with 99% classified as nonlinear~~ (Figure 3k), confirming their capability to trap and advect water mass during their lifespan. In the nonlinearity regime ($\beta > 1$), equatorward-moving CEs constitute ~~70~~72% of the total cross-frontal CEs, and ~~65~~64% of the total cross-frontal AEs are poleward-moving ones (Figure 3k)~~ (not shown)~~. In the high nonlinearity regime ($\beta > 5$), the proportion of CEs is notably higher than AEs, consistent with the greater dynamic vigor of CEs observed in the above analyses. Therefore, the cross-frontal transport achieved by eddies, primarily equatorward-moving CEs and poleward-moving AEs, can facilitate the redistribution of distinct source water masses and reduce~~mitigate~~ thermohaline gradients across frontal zones.

~~–Quantitative analysis of CFE types reveals distinct latitudinal patterns in eddy behavior (Table 1). The overall proportion of eddies that complete a full frontal crossing is obtained by summing the percentages of complete anticyclonic eddies (AEs) and cyclonic eddies (CEs) at each front. This proportion is less than a quarter (ranging from 3.99% to 12.92%) and decreases poleward, being highest at the Subantarctic Front (SAF: 5.14% AEs + 7.78% CEs = 12.92%), followed by the Northern Boundary (NB: 11.65%) and lowest at the Southern Boundary (SB: 3.99%). At most fronts, CEs constitute a larger fraction of complete CFEs than AEs. The maximum difference in favor of CEs is 2.56% (CEs: 7.78% vs. AEs: 5.14% at the SAF).~~

~~Quantitative analysis of CFE types reveals distinct latitudinal patterns in eddy behavior (Table 1). Less than half (3.99–12.92%) complete full frontal crossing, with success rates decreasing poleward (12.92% at SAF, 11.65% at NB, vs. 3.99% at SB). CEs largely outperform AEs (maximum 2.56% difference at SAF). Over half of the eddies undergo generation or dissipation within frontal zones, and this proportion increases towards higher latitudes. Among the front-generated eddies, AEs slightly outnumber CEs at SAF and PF, while CEs dominate at the other fronts. Dissipation follows similar patterns, where AEs outnumber CEs only at SAF. Transient frontal eddies also occur more frequently at the higher-latitude fronts, with CEs generally exceeding AEs (except at SAF and PF). The latitudinal differences in eddy behavior, particularly the declined complete CFEs but the enhanced partial and transient frontal crossing eddies in weaker fronts (e.g., SACCF, SB), highlight the critical role of frontal jet instability in modulating eddy generation, transport efficiency, and cross-frontal exchange.~~

Cross-frontal CEs and AEs show similar distributions in lifespan, propagation distance, and size (Figure 4). Both types show a steep decline in abundance with increasing lifespan. Eddies with lifespans ≤ 50 days dominate, constituting 55% of the total eddy population, while only 3% exceed 200 days (Figure 4a). Propagation distances are confined predominantly to ≤ 400 km (56% of total CFEs). CEs slightly outnumber AEs at longer distances (400–1000 km; Figure 4b). Size distributions reveal that ~75% of the total sample have mean radii of 30–50 km (Figure 4c). Notably, CEs dominate at smaller radii (< 50 km), while AEs prevail among larger eddies. This distribution pattern is consistent with maximum radius statistics (Figure 4d). These CFE characteristics align with previously reported eddies in the Pacific sector (Duan et al., 2016).

Subsequently, we found distinct characteristics among types regarding their behaviors, when dividing the CFEs into partial CFEs, generated within and subsequently transported away (Type 1) and transported into and dissipated within the frontal zones (Type 2); transient CFEs, both generated and dissipated within the same frontal zone (Type 3); and complete CFEs, experiencing pre-crossing, crossing, and post-crossing phases (Type 4). Transient CFEs dominate numerically, accounting for 48% of all CFEs, and partially generated and dissipated CFEs constitute 23% and 20%, respectively (Figure 4a–d). These proportions collectively indicate that the frontal zones primarily act as terminal/starting areas for eddy life cycles, rather than a simple transit pathway. The proportion of transient CFEs falling within low-value parameter ranges is substantially higher than that of the other types: 59% of these eddies have lifespans ≤ 40 days and propagation distances ≤ 300 km, as well as 58% have mean radius ≤ 43 km and 63% have maximum radius ≤ 60 km. These values confirm the intrinsic nature of transient eddies as "generated and dissipated locally", and reveal the constraining role of the frontal system on eddy evolution. In stark contrast, completely transported CFEs exhibit markedly different dynamical characteristics: 81%

have lifespans > 40 days, 90% propagate > 300 km, and 68% have maximum radii > 60 km, indicating that these eddies have completely escaped the constraints of the local frontal environment and possess the capability for long-distance cross-frontal transport. Notably, among completely transported CFEs, small-scale CEs dominate significantly, with CEs accounting for 63%, while AEs account for only 37% for eddies with mean radii of 30–50 km and maximum radii < 70 km. This polarity bias suggests that small-scale CEs may possess higher transport efficiency in cross-frontal material and energy exchange due to their unique dynamical structure.

Quantitative analysis of CFE types reveals distinct frontal-zone behaviors (Table 1). Transient eddies (Type 3) account for the largest proportion overall (> 40% by summing the transient AEs and CEs at each front), particularly at the two weaker southern fronts (SACCF and SB). Their proportions are lower at the SAF and PF, indicating that these two major fronts host more eddies that interact with areas outside the frontal zone during their lifecycle. For partially front-generated eddies (Type 1), both AEs and CEs exhibit relatively high proportions at the SAF and PF. At the southern SACCF and SB, however, the proportion of AEs drops markedly, whereas CEs show no such reduction. Among partially front-dissipated eddies (Type 2), the three northern fronts consistently show a higher proportion of CEs than AEs. At the two southern fronts, the pattern reverses, CE proportions decline sharply, ~~leading to~~causing a higher proportion of AEs. This suggests that in the southern fronts, local cross-frontal CEs are more readily generated and propagated outward, while being relatively resistant to dissipation.

Regarding the partial CFEs, the proportion of front-generated AEs consistently exceeds that of front-dissipated AEs (except the SB), indicating that AEs are more likely to be generated within the fronts than to dissipate locally, particularly at the three northern fronts. For complete CFEs (Type 4), the proportion of AEs decreases with frontal latitude, while CEs reach their maximum proportions at the SAF and PF. These results demonstrate that different CFE types exhibit distinct behaviors when interacting with each front, shaped by frontal dynamics and latitudinal position.

~~Front-generated or dissipated eddies typically exhibit relatively short lifespans (lifespan ≤ 40 days: 50% of generated eddies, 51% of dissipated eddies), limited propagation distances (predominantly confined to ≤ 300 km: 49% generated, 50% dissipated), and small radii (mean radii ≤ 43 km: 55% generated, 55% dissipated; maximum radius ≤ 60 km: 57% generated, 58% dissipated), with very few exceptions in high-value parameter ranges (Figure 4a–d). Conversely, completely transported CFEs display markedly longer lifespans display marked longer lifespans (lifespan > 40 days: 81% of the complete CFEs), greater propagation distances (> 300 km: 90%), and larger radii (mean radii > 43 km: 59%; maximum radii > 60 km: 68%). It's notable that CEs~~

~~significantly outnumber AEs among small-scale completely transported CFEs (mean radii: 30–50 km; maximum radii < 70 km), with 63% versus 37%. The higher abundance of small-scale CEs suggests their efficiency in cross-frontal transport processes.~~

Over the 22 years,~~ both~~ the counts of poleward- and equatorward-moving eddies show pronounced interannual variability (Figure 4e). The annual abundance hierarchy, equatorward CEs > poleward AEs > equatorward AEs > poleward CEs, mirrors the total distribution in Figure 2b.~~ and is primarily constituted by completely transported CFEs (Figure 5d), underscoring the enhanced capacity of equatorward CEs and poleward AEs for sustained cross-frontal propagation. In contrast, partial or transient CFEs exhibit no clear polarity preferences, although CEs are slightly dominant equatorward types and AEs prevail among poleward types in most years (Figure 5a–c).~~ In terms of EKE_T,

~~The~~ CEs consistently exhibit approximately 1.5-fold greater EKE_T than AEs (Figure 4f), consistent with their longer propagation distances and higher linearity (Figure 3). While the increasing trend in CEs' EKE_T~~ shows~~ is not statistically ~~a non-~~significant ~~increasing trend~~ overall (1.77 ± 1.81) × 10^6 m^4 s^{-2} yr^{-1}~~10^6 m^4 s^{-2} yr^{-1}~~ (p = 0.051), this result is influenced by an anomalously low value in 2017~~ value ~~,~~that~~ coinciding~~es~~ with an *EKE* minimum reported by Fu et al. (2023) in the central Pacific sector. E~~When e~~xcluding this outlier yields a significant trend ~~, CEs' EKE_T trend becomes statistically significant with~~of (2.27 ± 1.45) × 10^6 m^4 s^{-2} yr^{-1}~~m^{4}s^{-2}yr^{-1}~~ (p = 0.003). In contrast, AEs' EKE_T displays a ~~significant~~robust increase ~~ing~~by~~ trend of~~ (2.27 ± 0.94) × 10^6 m^4 s^{-2} yr^{-1}~~m^{4}s^{-2}yr^{-1}~~ (p < 0.001). These results indicate that both eddy polarities contribute to the long-term EKE_T rise~~for both polarity eddies increases over the 22 years~~, with CEs exhibiting greater interannual variability. As established in Figure 2, equatorward-propagating CEs and poleward-propagating AEs dominate cross-frontal eddy abundance. Their EKE_T signals~~Examining their EKE_T trends reveals that~~ are~~they exhibit~~ substantially stronger than~~signals compared to~~ those of~~for~~ the overall CFE population, with significant~~with~~ increasing trends~~ for equatorward CEs~~ of (2.43 ± 2.45) × 10^6 m^4 s^{-2} yr^{-1} (p = 0.045) for equatorward CEs and~~ poleward AEs of~~ (2.64 ± 1.39) × 10^6 m^4 s^{-2} yr^{-1}~~m^{4}s^{-2}yr^{-1}~~ (p < 0.001) for poleward AEs. Thus, beyond their numerical dominance, these two subsets also govern the *EKE* level of CFEs and its intensification over the study period.~~–~~

~~–~~More specifically, all CFE types exhibit pronounced interannual variability and follow the same abundance hierarchy observed in Figure 4e in annual counts, with CEs dominating equatorward-moving eddies and AEs prevailing among poleward-moving ones (Figure 5a–d). Among the four types, complete CFEs of both polarities show the largest annual mean EKE_T, and display statistically significant increases over the study period with~~the observed increase in annual mean EKE_T is primarily driven by complete CFEs, with CEs and AEs showing~~

~~significant trends of~~ (4~~3~~.16~~3~~ ± 3.54~~17~~) × 10^6 $m^4\ s^{-2}\ yr^{-1}$~~$m^4 s^{-2} yr^{-1}$~~ (p = 0.024~~04~~) for CEs and (3~~2~~.17~~59~~ ± 2.49~~66~~) × 10^6 ~~$m^4 s^{-2} yr^{-1}$~~$m^4\ s^{-2}\ yr^{-1}$ (p = 0.015~~5~~) for AEs, respectively (Figure 5h). The dominant contributors to this enhancement are the same subsets that dominate abundance, equatorward-moving CEs and poleward-moving AEs, underscoring their role as the primary EKE_T source for complete CFEs. –In contrast, partial and transient CFEs~~or transient CFEs~~ exhibit substantially~~show~~ lower EKE_T levels, with~~ and~~ transient eddies showing the weakest energy content. –Most of their increasing trends are not statistically ~~no ~~significant~~t trends~~ (Figure 5a–c), with the notable exception of transient AEs, which display a significant EKE_T increase (Figure 5c)~~ (Figure 5a–c)~~.–

The relative contribution of each type to the total annual EKE_T reveals distinct energy compensation patterns between AEs and CEs (Figure 5i, j). For AEs, the primary energy compensation occurs between Type 1 (front-generated) and Type 4 (complete frontal-crossing) eddies (correlation coefficient R = −0.59; p = 0.003), indicating that enhanced activity of partially frontal-generated AEs tends to suppress complete frontal-crossing AEs, and vice versa. A secondary compensation is between Type 2 and Type 3 (R = −0.46; p = 0.027). For CEs, the dominant compensation is between Type 3 (transient) and Type 4 (complete) eddies (R = −0.66; p < 0.001), with a modest compensation between Type 1 and Type 4 (R = −0.44; p = 0.032). These results suggest that more energetic complete CFEs tend to coexist with reduced activity of either partially frontal-generated or transient eddies. This compensatory relationship is critical for understanding mesoscale eddy-front interactions, particularly during the period of elevated EKE_T in complete CFEs.~~The energy contrast between complete CEs and complete AEs is more pronounced than in other eddy types. The intensification pattern is consistent in mean EKE data (Figure S1 in Supplementary Materials), which shows a greater enhancement in CEs. These results indicate the rise in CFE activity from 2000–2022 is largely attributable to equatorward-propagating complete CEs and poleward-propagating complete AEs, the most energetic two types. Notably, the time series demonstrates a decoupling between EKE intensity and eddy abundance, exemplified by 2017 when CE abundance exceeded AE, yet their EKE_T dropped below AE levels (Figure 4e, f).~~

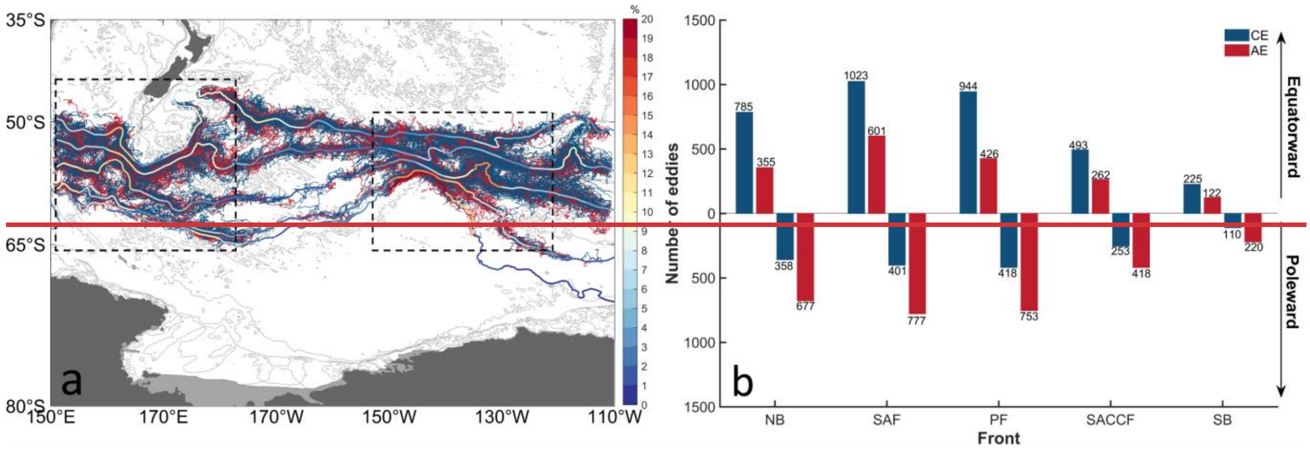
35°S
50°S
65°S
80°S
150°E
170°E
170°W
150°W
130°W
110°W
a
%
20
19
18
17
16
15
14
13
12
11
10
9
8
7
6
5
4
3
2
1
0
b
Number of eddies
1500
1000
500
0
500
1000
1500
CE
AE
Equatorward
Poleward
785
355
358
677
1023
601
401
777
944
426
418
753
493
262
253
418
225
122
110
220
NB
SAF
PF
SACCF
SB
Front

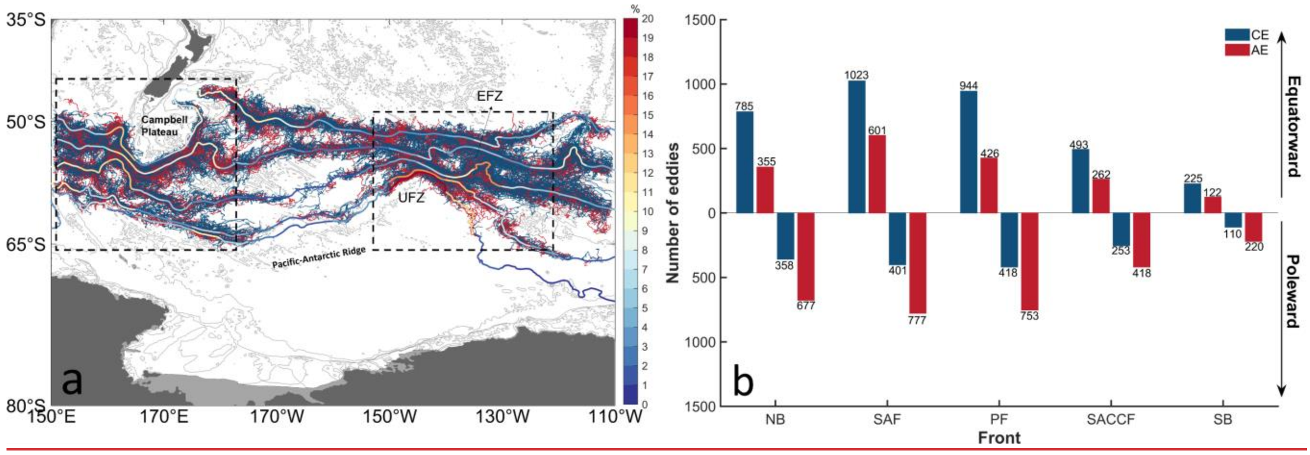
35°S
50°S
65°S
80°S
150°E
170°E
170°W
150°W
130°W
110°W
Campbell Plateau
EFZ
UFZ
Pacific-Antarctic Ridge
a
%
20
19
18
17
16
15
14
13
12
11
10
9
8
7
6
5
4
3
2
1
0
b
Number of eddies
1500
1000
500
0
500
1000
1500
CE
AE
Equatorward
Poleward
785
355
358
677
1023
601
401
777
944
426
418
753
493
262
253
418
225
122
110
220
NB
SAF
PF
SACCF
SB
Front

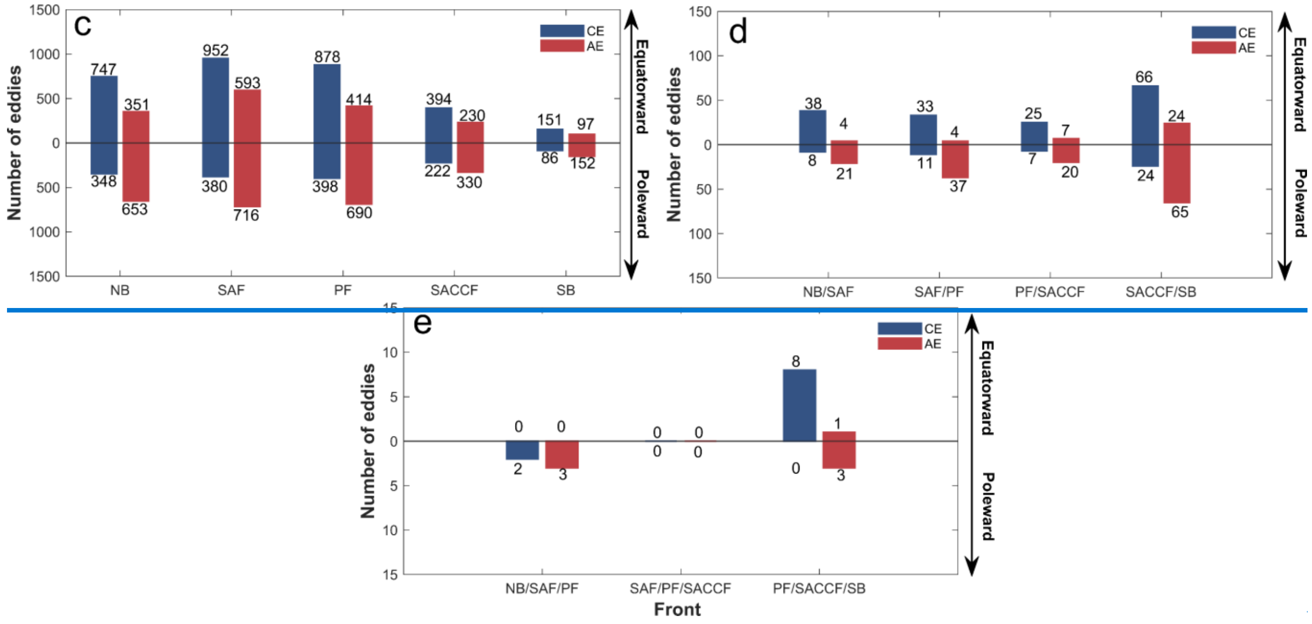

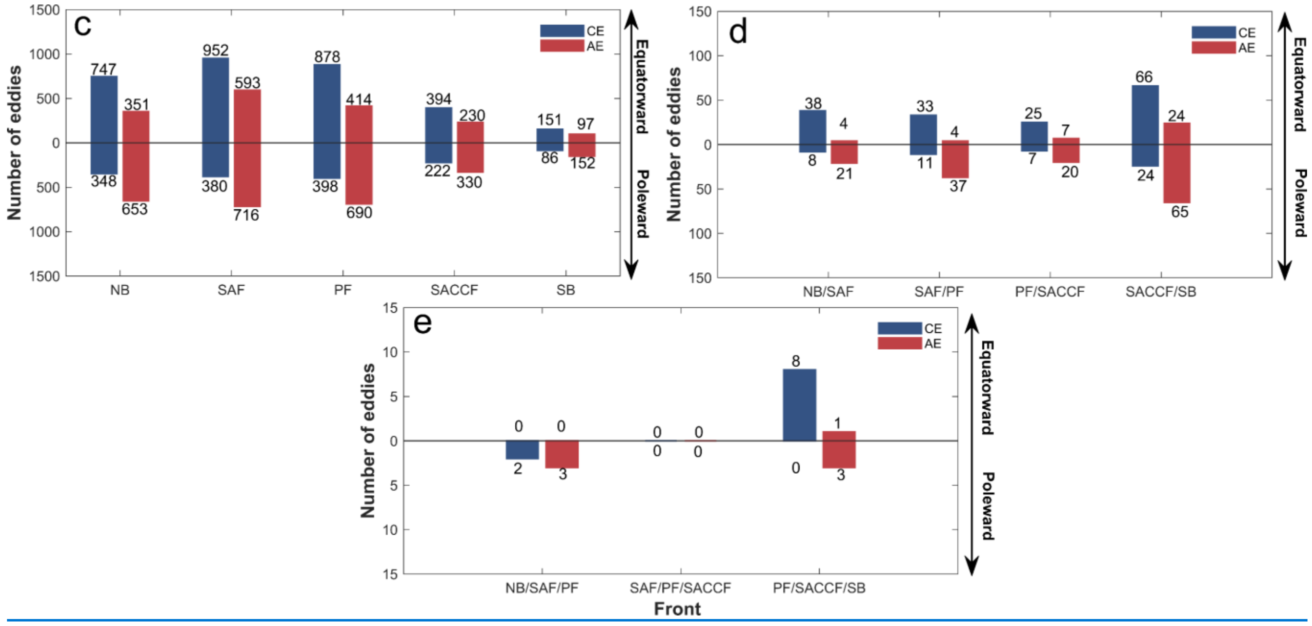

Figure 2. CFE trajectories and statistics of eddy counts. (a) CFE trajectories. The color along each front represents the relative occurrence of CFEs (%) per 5° latitudinal bin. The framed regions denote the area where active CFE activity occurs. (b) Total number of CFEs, divided into types of equatorward and poleward directions, shown as a function of the different ACC fronts; (c~~)~~–~~(~~e) Numbers of single-, double-, and triple-frontal crossing CFEs, respectively. Red represents anticyclonic eddies (AEs) and dark blue denotes cyclonic eddies (CEs).~~ Note: The Northern Boundary (NB) is the streamline defining the northern limit of the ACC, following Park et al. (2019).~~

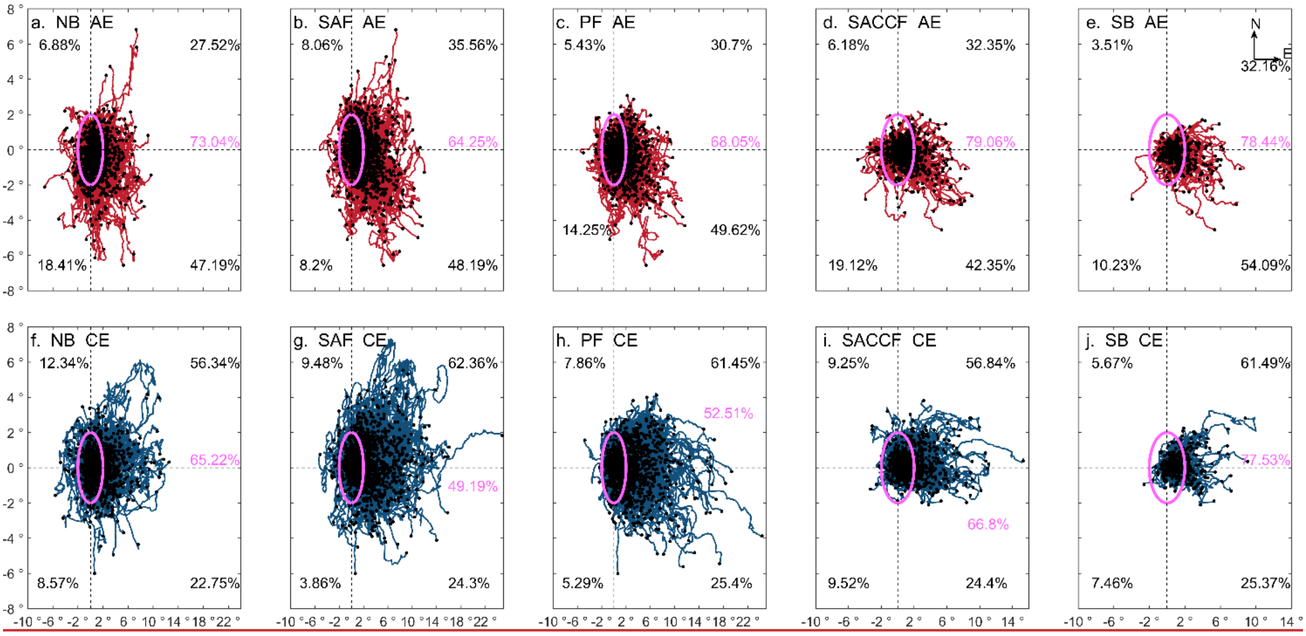
a. NB AE
6.88%
27.52%
73.04%
18.41%
47.19%
b. SAF AE
8.06%
35.56%
64.25%
8.2%
48.19%
c. PF AE
5.43%
30.7%
68.05%
14.25%
49.62%
d. SACCF AE
6.18%
32.35%
79.06%
19.12%
42.35%
e. SB AE
N
E
3.51%
32.16%
78.44%
10.23%
54.09%
f. NB CE
12.34%
56.34%
65.22%
8.57%
22.75%
g. SAF CE
9.48%
62.36%
49.19%
3.86%
24.3%
h. PF CE
7.86%
61.45%
52.51%
5.29%
25.4%
i. SACCF CE
9.25%
56.84%
66.8%
9.52%
24.4%
j. SB CE
5.67%
61.49%
77.53%
7.46%
25.37%
8 °
6 °
4 °
2 °
0 °
-2 °
-4 °
-6 °
-8 °
-10 ° -6 ° -2 ° 2 ° 6 ° 10 ° 14 ° 18 ° 22 °
-10 ° -6 ° -2 ° 2 ° 6 ° 10 ° 14 °

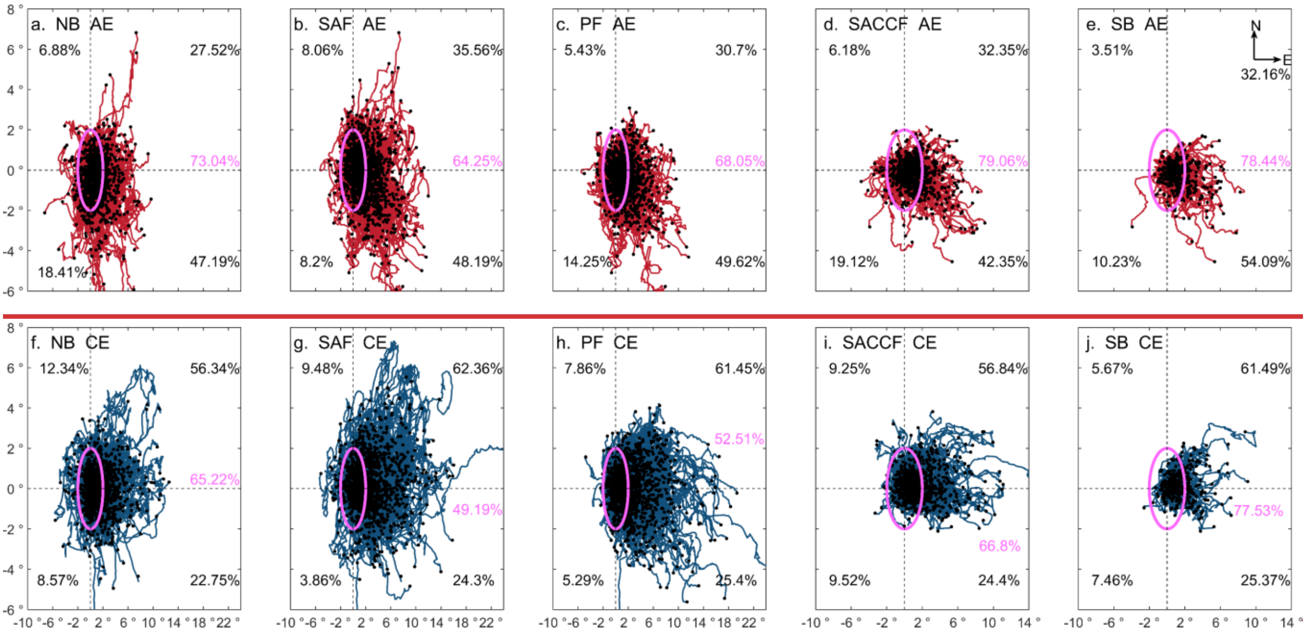
a. NB AE
6.88%
27.52%
73.04%
18.41%
47.19%
b. SAF AE
8.06%
35.56%
64.25%
8.2%
48.19%
c. PF AE
5.43%
30.7%
68.05%
14.25%
49.62%
d. SACCF AE
6.18%
32.35%
79.06%
19.12%
42.35%
e. SB AE
N
E
3.51%
32.16%
78.44%
10.23%
54.09%
f. NB CE
12.34%
56.34%
65.22%
8.57%
22.75%
g. SAF CE
9.48%
62.36%
49.19%
3.86%
24.3%
h. PF CE
7.86%
61.45%
52.51%
5.29%
25.4%
i. SACCF CE
9.25%
56.84%
66.8%
9.52%
24.4%
j. SB CE
5.67%
61.49%
77.53%
7.46%
25.37%
8 °
6 °
4 °
2 °
0 °
-2 °
-4 °
-6 °
-10 ° -6 ° -2 ° 2 ° 6 ° 10 ° 14 ° 18 ° 22 °
-10 ° -6 ° -2 ° 2 ° 6 ° 10 ° 14 °

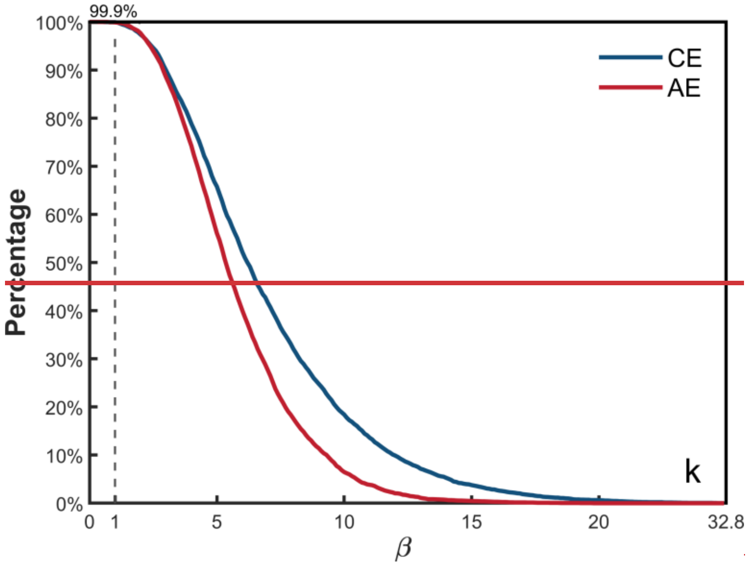

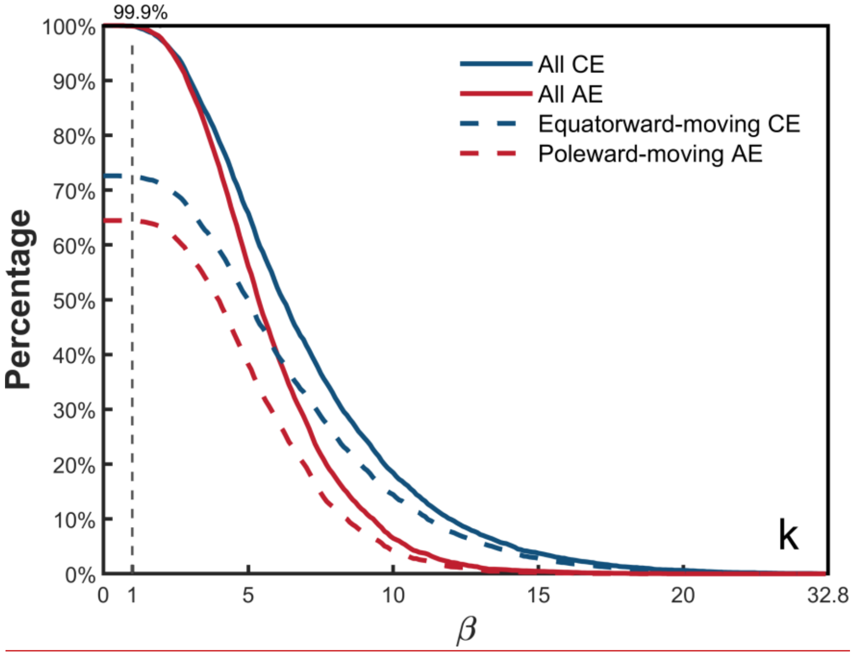

Figure 3. Relative movement trajectories of CFEs (a–j) and the percentage distribution of eddy nonlinearity *β* (k). In (a–j), black percentages represent the proportion of eddies moving in different quadrant directions calculated based on the end point of the trajectory, and purple percentages indicate the proportions of eddies with movement distances within a 2° range, with the coordinate origin (0°, 0°) denoting the eddies' generation locations. Note that eddies crossing multiple fronts may appear repeatedly at different frontal positions in this analysis.

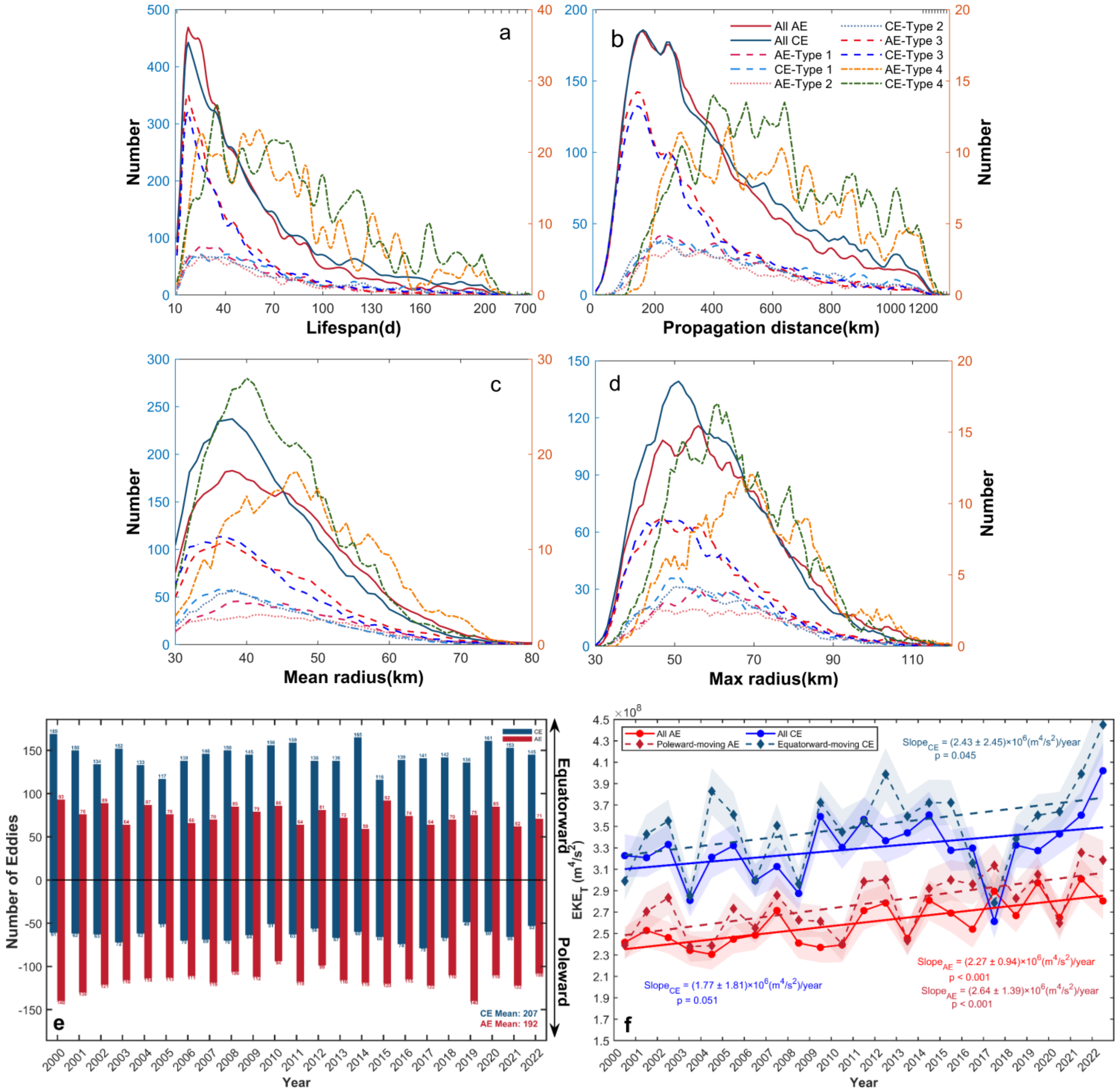
a
Number
Lifespan(d)
b
Propagation distance(km)
Number
All AE
All CE
AE-Type 1
CE-Type 1
AE-Type 2
CE-Type 2
AE-Type 3
CE-Type 3
AE-Type 4
CE-Type 4
c
Mean radius(km)
d
Max radius(km)
e
Number of Eddies
CE
AE
Equatorward
Poleward
CE Mean: 207
AE Mean: 192
Year
f
EKE_T (m^4/s^2)
×10^8
All AE
All CE
Poleward-moving AE
Equatorward-moving CE
Slope_CE = (2.43 ± 2.45)×10^6(m^4/s^2)/year
p = 0.045
Slope_AE = (2.27 ± 0.94)×10^6(m^4/s^2)/year
p < 0.001
Slope_CE = (1.77 ± 1.81)×10^6(m^4/s^2)/year
p = 0.051
Slope_AE = (2.64 ± 1.39)×10^6(m^4/s^2)/year
p < 0.001
Year

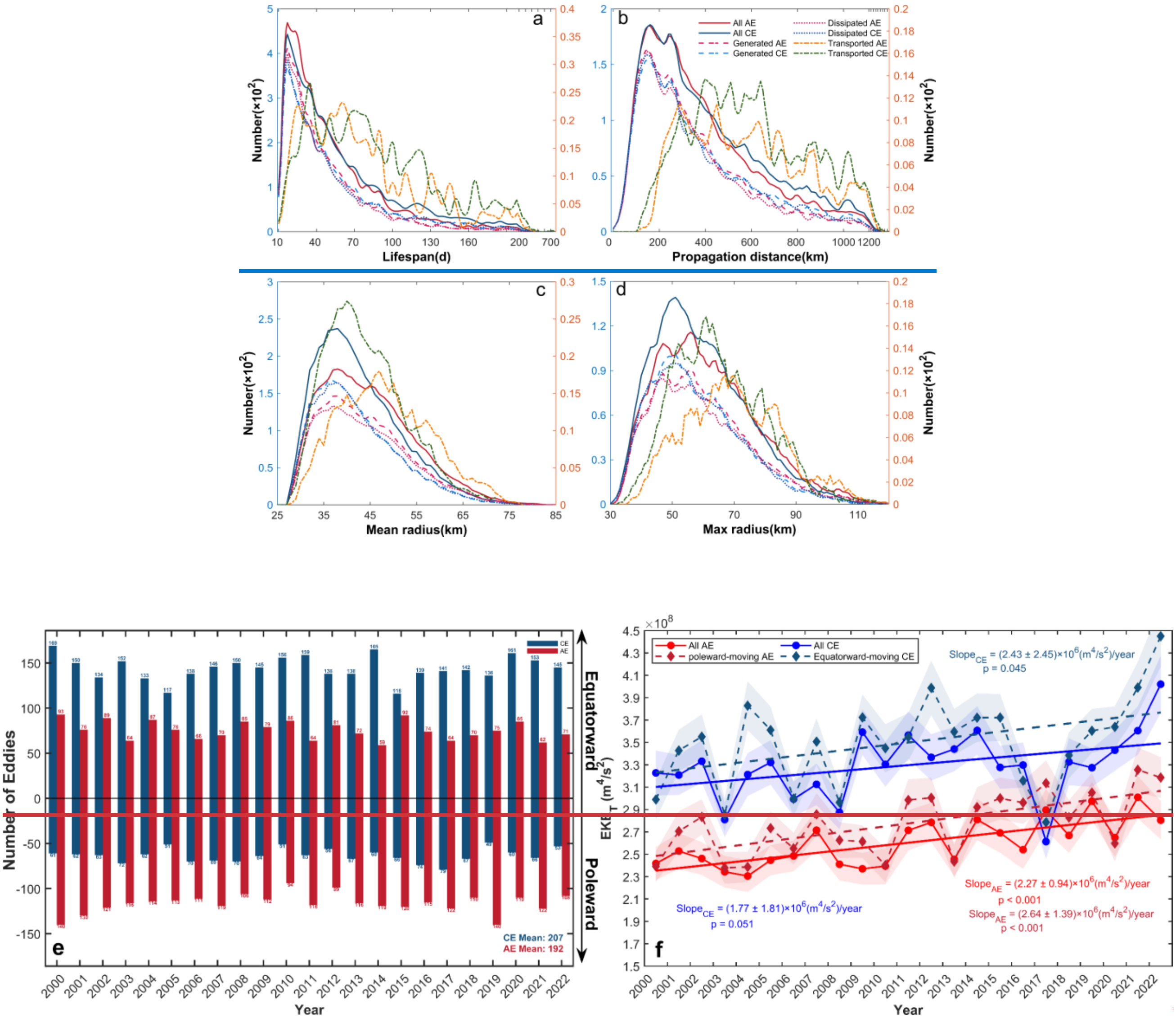

Figure 4. Statistical characteristics of different types of CFEs (a–d), ~~and~~ time series of annual CFE counts (e), and annual mean *EKE_T* (f). Eddy counts according to (a) eddy lifespan, (b) propagation distance, (c) mean radius over lifespan, and (d) maximum radius in the lifespan. ~~The x-axes in (a) and (b) are plotted on a nonlinear scale. This is done to compress the long-tail distribution, thereby providing a clearer view of the region where most data points are concentrated. Note the x-axis in a b are not equidistant at higher values.~~ In (a–d), "All" represents all CFEs, "Type 1~~Generated~~" denotes eddies front-generated and subsequently transported away~~eddies~~, "Type 2~~Dissipated~~" indicates eddies transported into the frontal zone and ~~front~~ dissipated there~~eddies~~, "Type 3" represents eddies generated and dissipated within the same frontal zone, and "Type 4~~Transported~~" shows complete CFEs experiencing pre-crossing, crossing and post-crossing phases.~~, A dual y-axis format is used, with~~ T~~t~~he left Y-~~-~~axis is for the first three subsets, and~~ a separately sealed~~ the right axis is for the Type 4 eddies~~"Transported" group~~ to clarify their~~its~~ distribution. The x-axes in (a) and (b) are compressed at higher values.~~plotted on a nonlinear scale by compressing the long-tail distribution.~~ In (e), all-year mean counts of CEs and AEs are indicated at the~~right~~ bottom right. In (f), the annual mean *EKE_T* for all AEs and CEs and the linear trends are depicted by~~ light~~ dots, red and~~ light~~ blue solid lines, respectively~~, with their linear trends indicated by solid lines in the same colors~~. T~~Superimposed are t~~he extracted subsets of poleward-moving AEs and equatorward-moving CEs are~~,~~ depicted by diamonds,~~ light~~ red and~~ light~~ blue dashed lines, respectively~~with their linear trends shown by dashed lines in the same respective colors~~. Error shadings represent ± 1 standard deviation~~one standard deviation~~, and slope values are given with ± 95% confidence intervals.

Table 1. Proportions of numbers of different eddy types relative to the total number of CFEs at each frontal zone.

Type	**Eddy polarity**	**NB**	**SAF**	**PF**	**SACCF**	**SB**
(1) Front-generated eddies	AE	11.03%	12.21%	12.00%	8.84%	7.68%
	CE	10.11%	12.81%	12.59%	12.69%	10.49%
(2) Front-dissipated eddies	AE	8.41%	9.17%	9.21%	7.22%	9.45%
	CE	12.78%	11.74%	13.58%	6.52%	5.91%
(3) Transient frontal eddies	AE	22.71%	22.66%	20.43%	29.18%	31.17%
	CE	24.47%	18.49%	20.54%	30.37%	31.31%
(4) Complete CFEs	AE	5.29%	5.14%	4.76%	2.45%	2.22%
	CE	5.20%[1][2]	7.78%	6.89%	2.73%	1.77%

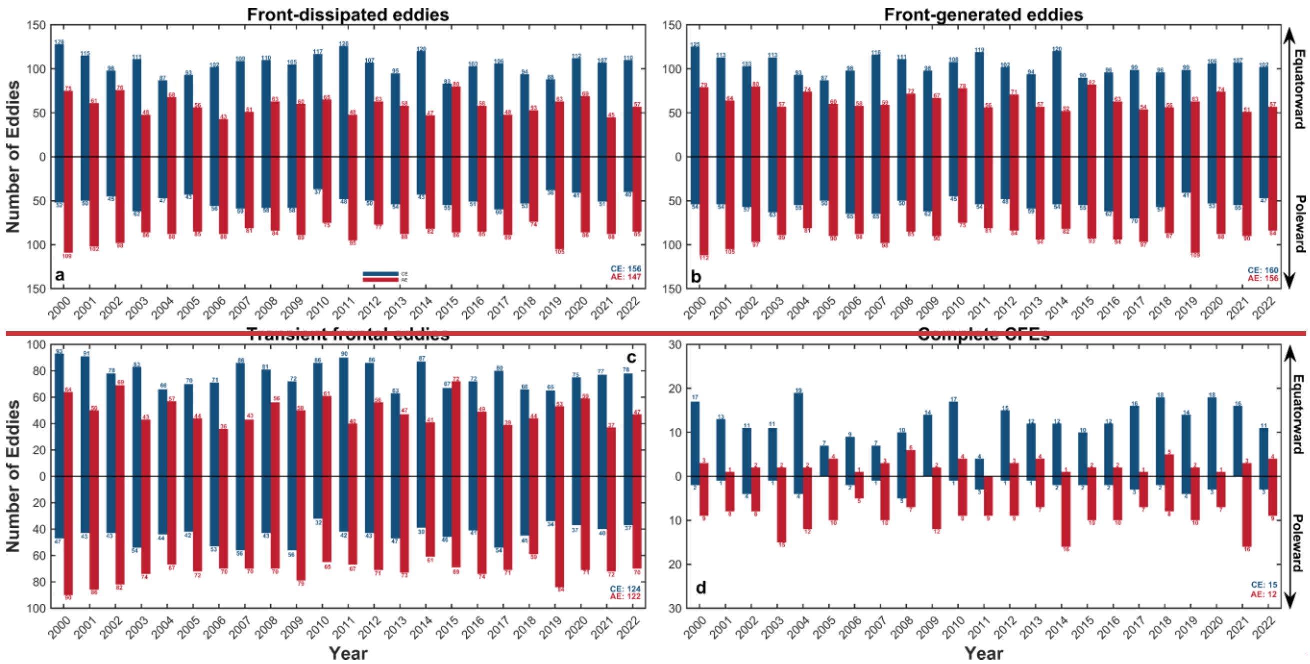
Front-dissipated eddies
Front-generated eddies
Transient frontal eddies
Complete CFEs
Number of Eddies
Year
Equatorward
Poleward
a
b
c
d
CE
AE
CE: 156
AE: 147
CE: 160
AE: 156
CE: 124
AE: 122
CE: 15
AE: 12

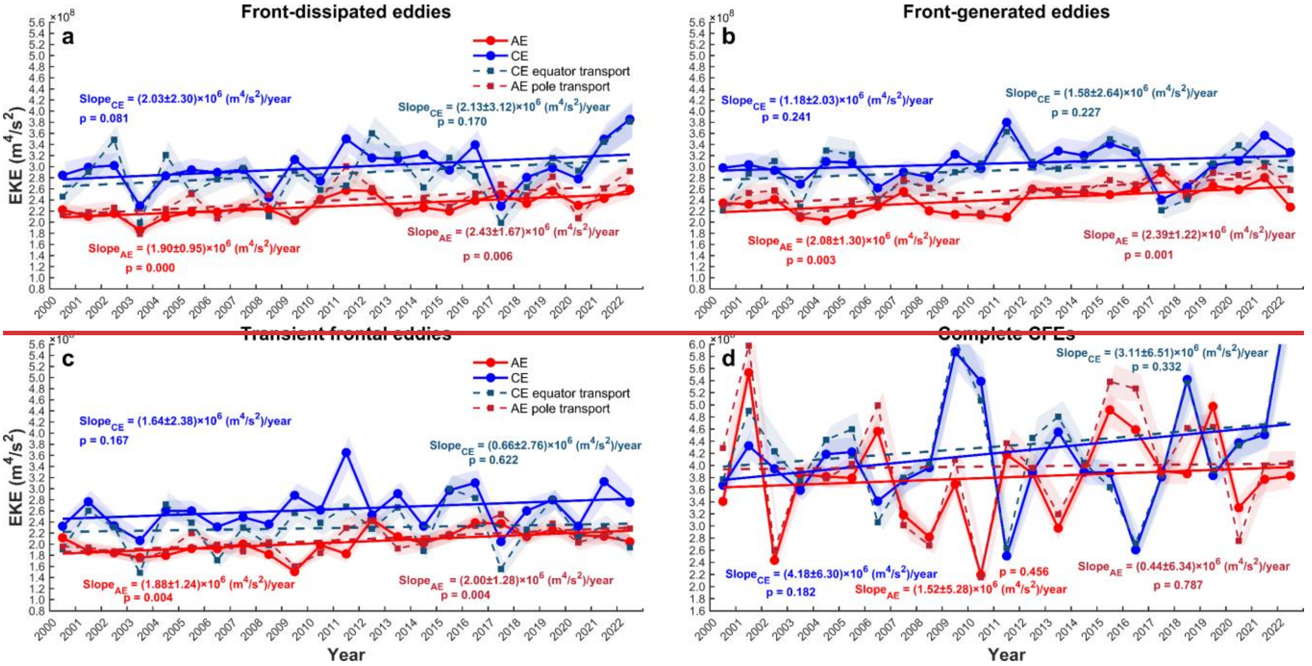
Front-dissipated eddies
Front-generated eddies
Transient frontal eddies
Complete CFEs
a
b
c
d
EKE (m⁴/s²)
×10⁸
Year
AE
CE
CE equator transport
AE pole transport
Slope_CE = (2.03±2.30)×10⁶ (m⁴/s²)/year
p = 0.081
Slope_CE = (2.13±3.12)×10⁶ (m⁴/s²)/year
p = 0.170
Slope_AE = (1.90±0.95)×10⁶ (m⁴/s²)/year
p = 0.000
Slope_AE = (2.43±1.67)×10⁶ (m⁴/s²)/year
p = 0.006
Slope_CE = (1.18±2.03)×10⁶ (m⁴/s²)/year
p = 0.241
Slope_CE = (1.58±2.64)×10⁶ (m⁴/s²)/year
p = 0.227
Slope_AE = (2.08±1.30)×10⁶ (m⁴/s²)/year
p = 0.003
Slope_AE = (2.39±1.22)×10⁶ (m⁴/s²)/year
p = 0.001
Slope_CE = (1.64±2.38)×10⁶ (m⁴/s²)/year
p = 0.167
Slope_CE = (0.66±2.76)×10⁶ (m⁴/s²)/year
p = 0.622
Slope_AE = (1.88±1.24)×10⁶ (m⁴/s²)/year
p = 0.004
Slope_AE = (2.00±1.28)×10⁶ (m⁴/s²)/year
p = 0.004
Slope_CE = (3.11±6.51)×10⁶ (m⁴/s²)/year
p = 0.332
Slope_CE = (4.18±6.30)×10⁶ (m⁴/s²)/year
p = 0.182
Slope_AE = (1.52±5.28)×10⁶ (m⁴/s²)/year
p = 0.456
Slope_AE = (0.44±6.34)×10⁶ (m⁴/s²)/year
p = 0.787

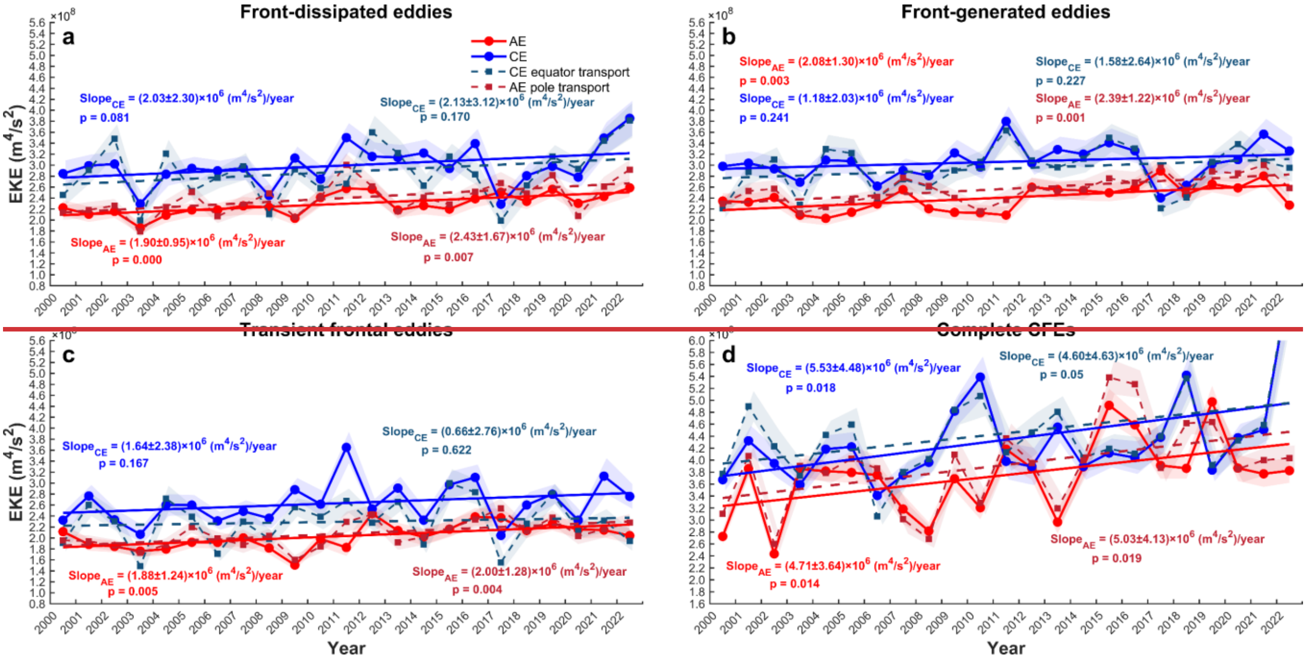
Front-dissipated eddies
a
×10^8
EKE (m^4/s^2)
AE
CE
CE equator transport
AE pole transport
Slope_CE = (2.03±2.30)×10^6 (m^4/s^2)/year
p = 0.081
Slope_CE = (2.13±3.12)×10^6 (m^4/s^2)/year
p = 0.170
Slope_AE = (1.90±0.95)×10^6 (m^4/s^2)/year
p = 0.000
Slope_AE = (2.43±1.67)×10^6 (m^4/s^2)/year
p = 0.007
Front-generated eddies
b
Slope_AE = (2.08±1.30)×10^6 (m^4/s^2)/year
p = 0.003
Slope_CE = (1.18±2.03)×10^6 (m^4/s^2)/year
p = 0.241
Slope_CE = (1.58±2.64)×10^6 (m^4/s^2)/year
p = 0.227
Slope_AE = (2.39±1.22)×10^6 (m^4/s^2)/year
p = 0.001
Transient frontal eddies
c
EKE (m^4/s^2)
Slope_CE = (1.64±2.38)×10^6 (m^4/s^2)/year
p = 0.167
Slope_CE = (0.66±2.76)×10^6 (m^4/s^2)/year
p = 0.622
Slope_AE = (1.88±1.24)×10^6 (m^4/s^2)/year
p = 0.005
Slope_AE = (2.00±1.28)×10^6 (m^4/s^2)/year
p = 0.004
Complete CFEs
d
Slope_CE = (5.53±4.48)×10^6 (m^4/s^2)/year
p = 0.018
Slope_CE = (4.60±4.63)×10^6 (m^4/s^2)/year
p = 0.05
Slope_AE = (4.71±3.64)×10^6 (m^4/s^2)/year
p = 0.014
Slope_AE = (5.03±4.13)×10^6 (m^4/s^2)/year
p = 0.019
Year
Year

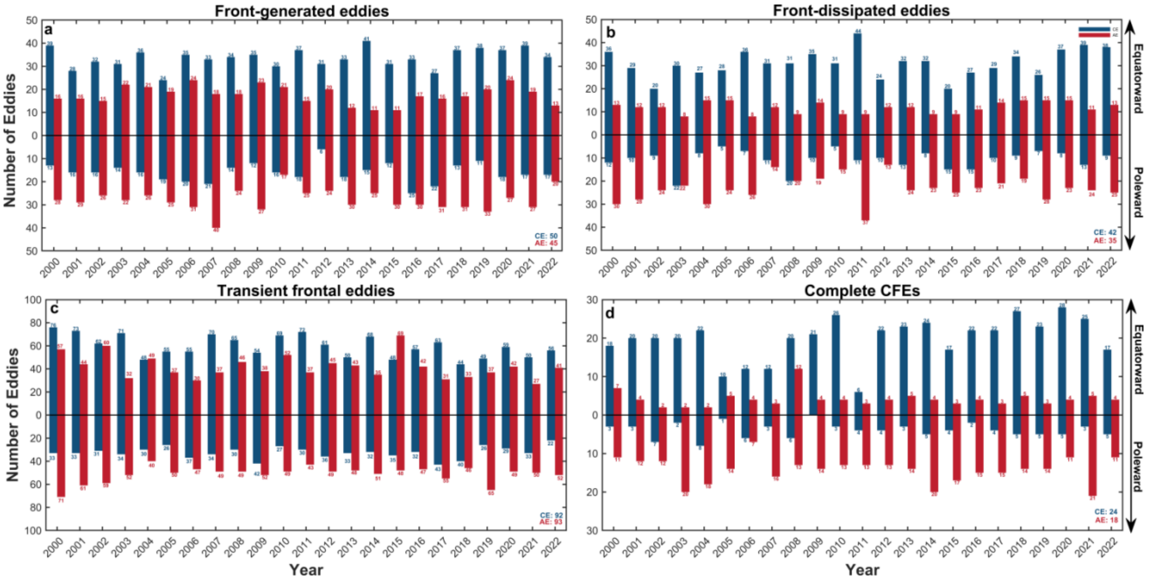
Front-generated eddies
a
Number of Eddies
CE: 50
AE: 45
Front-dissipated eddies
b
Equatorward
Poleward
CE: 42
AE: 35
Transient frontal eddies
c
Number of Eddies
CE: 92
AE: 93
Complete CFEs
d
Equatorward
Poleward
CE: 24
AE: 18
Year
Year

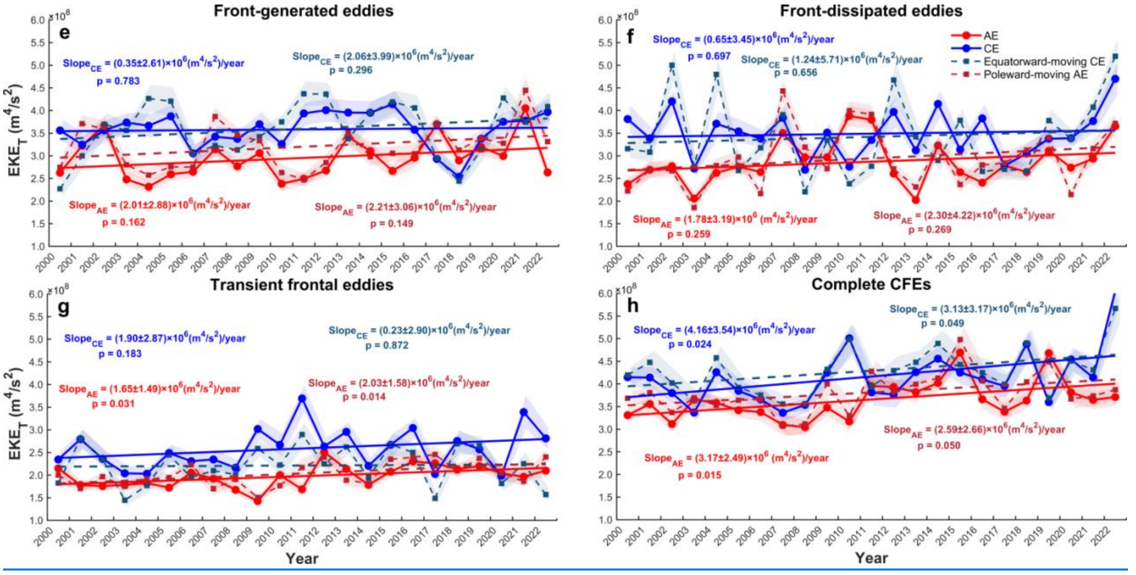
Front-generated eddies
e
×10^8
EKE_T (m^4/s^2)
Slope_CE = (0.35±2.61)×10^6(m^4/s^2)/year
p = 0.783
Slope_CE = (2.06±3.99)×10^6(m^4/s^2)/year
p = 0.296
Slope_AE = (2.01±2.88)×10^6(m^4/s^2)/year
p = 0.162
Slope_AE = (2.21±3.06)×10^6(m^4/s^2)/year
p = 0.149
Front-dissipated eddies
f
AE
CE
Equatorward-moving CE
Poleward-moving AE
Slope_CE = (0.65±3.45)×10^6(m^4/s^2)/year
p = 0.697
Slope_CE = (1.24±5.71)×10^6(m^4/s^2)/year
p = 0.656
Slope_AE = (1.78±3.19)×10^6 (m^4/s^2)/year
p = 0.259
Slope_AE = (2.30±4.22)×10^6(m^4/s^2)/year
p = 0.269
Transient frontal eddies
g
EKE_T (m^4/s^2)
Slope_CE = (1.90±2.87)×10^6(m^4/s^2)/year
p = 0.183
Slope_CE = (0.23±2.90)×10^6(m^4/s^2)/year
p = 0.872
Slope_AE = (1.65±1.49)×10^6(m^4/s^2)/year
p = 0.031
Slope_AE = (2.03±1.58)×10^6(m^4/s^2)/year
p = 0.014
Complete CFEs
h
Slope_CE = (4.16±3.54)×10^6(m^4/s^2)/year
p = 0.024
Slope_CE = (3.13±3.17)×10^6(m^4/s^2)/year
p = 0.049
Slope_AE = (2.59±2.66)×10^6(m^4/s^2)/year
p = 0.050
Slope_AE = (3.17±2.49)×10^6 (m^4/s^2)/year
p = 0.015
Year
Year

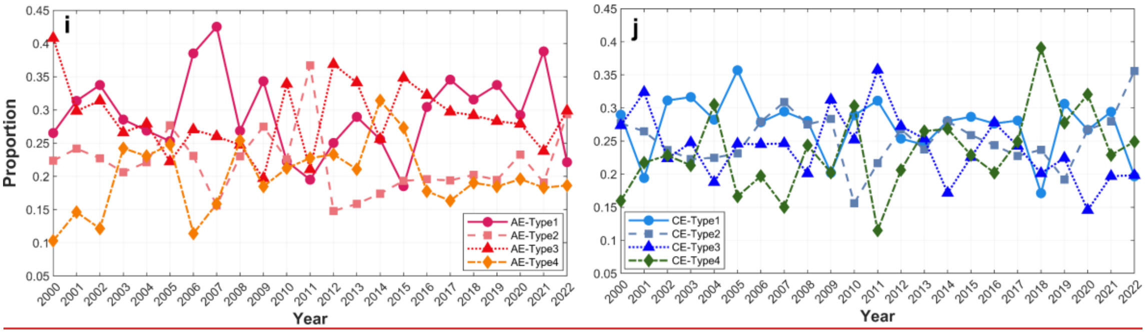

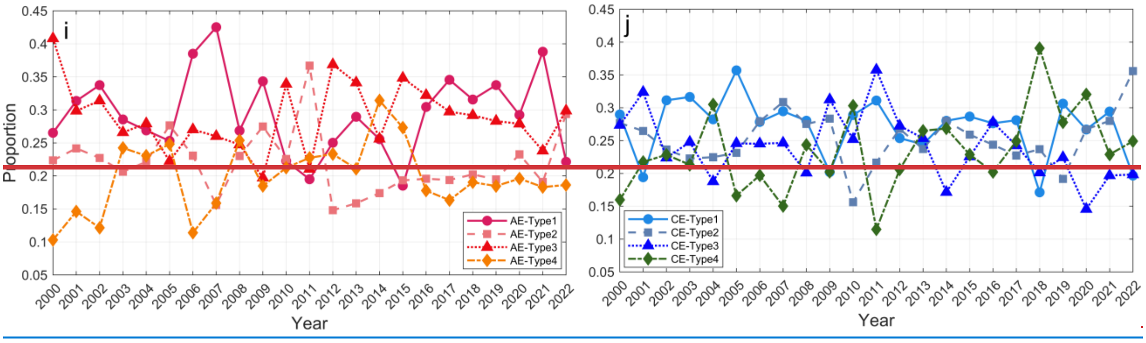

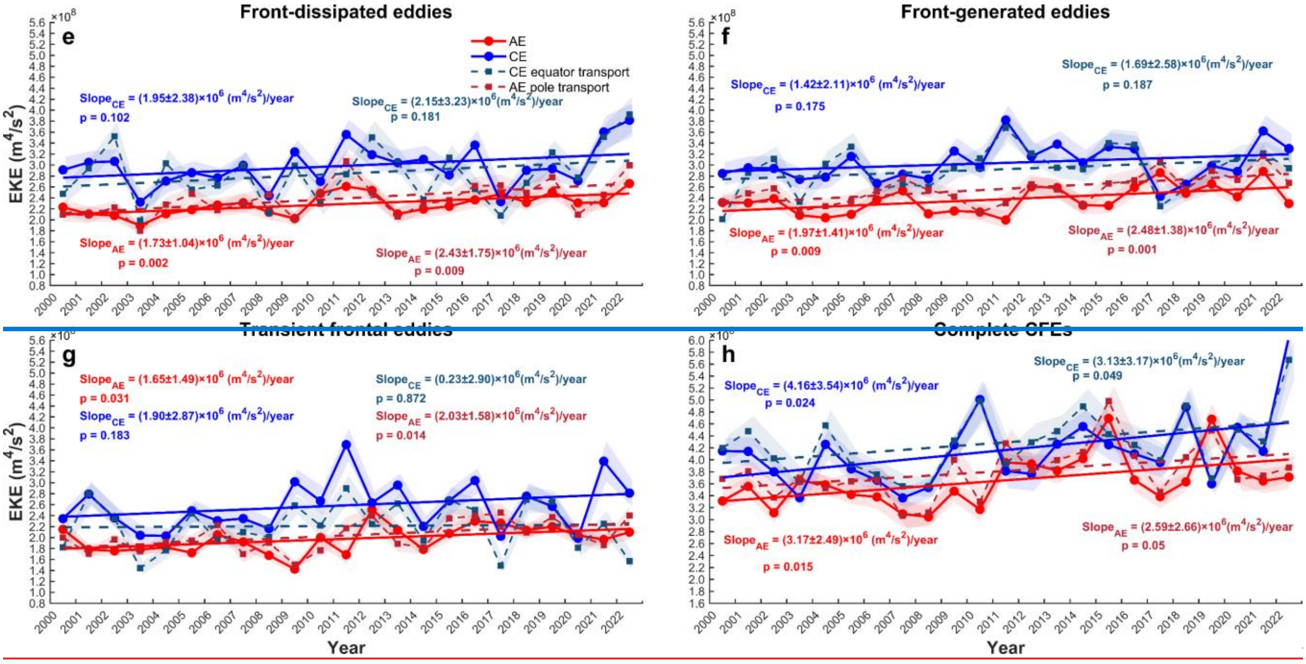

Figure 5. Annual s~~S~~tatistical characteristics of four types of CFEs, including their counts, mean EKE_T~~-~~, and proportions of the summed EKE_T relative to all EKE_T. ~~(a–d)~~ Time series of annual counts for (a) Front-generated~~dissipated~~ eddies (Type 1), (b) Front-dissipated~~generated~~ eddies (Type 2), (c) Transient frontal eddies (Type 3), and (d) Complete CFEs (Type 4). (e–h) A~~(e–h)a~~nnual mean EKE_T for these four types of eddies~~(e) Front-dissipated eddies, (f) Front-generated eddies, (g) Transient frontal eddies, and (h) Complete CFEs~~. (i, j) Annual summed EKE_T for each type relative to all EKE_T for total CFEs. In (a–d), all-year mean counts of CEs and AEs are indicated at the bottom right~~-bottom~~. In (e–h), the annual mean EKE_T for all AEs and CEs and the linear trends are depicted by dots, red and blue solid lines, respectively. The extracted subsets of poleward-moving AEs and equatorward-moving CEs are depicted by diamonds, red and blue dashed lines, respectively. Error shadings represent ± 1 standard deviation, and slope values are given with ± 95% confidence intervals.

~~**The dashed lines in (e–h) show the linear trends, with colors matching their respective time series. The slope values of the trends are provided with ±95% confidence intervals.**~~

3.2 ~~Variations in~~ EKE_T evolution of complete CFEs during frontal crossing

~~While~~Although only a small fraction of eddies complete full cross-frontal transport (Table 1;~~,~~ Figure 5), these energetic ~~eddies~~features, originating in non-frontal zones and crossing entire frontal boundaries, likely dominate long-distance heat and material exchange between inter-frontal zones. Their rising EKE_T underscores their increasingly important dynamic role, motivating a closer examination of EKE_T evolution during frontal crossing. ~~To quantify the influence of eddy-jet interactions on EKE in this type during frontal crossing, we analyzed the evolution of EKE_T across the three phases: pre-crossing, crossing, and post-crossing.~~ The Southern Hemisphere's intrinsic vorticity asymmetry (clockwise CEs vs. counterclockwise AEs) creates fundamental polarity differences in energy exchange when interacting with eastward frontal jets. Consequently~~Hence~~, eddies of opposing polarities and directions are expected to exhibit distinct patterns of EKE_T variability~~tion~~ during the cross-frontal transport.

C~~As shown in Figures 6 and 7, c~~omplete CFEs at the northern ACC ~~domains~~fronts,~~ encompassing the northern boundary (~~NB,~~) and the northern frontal jets (~~SAF, and~~,~~ PF,~~)~~ exhibit substantially~~significantly~~ higher EKE_T ~~values~~ than those at the southern fronts (SACCF, SB; Figures 6, 7)~~As shown in Figures 6 and 7, complete CFEs at the northern fronts (NB, SAF, PF) exhibit significantly higher EKE_T values than at the southern fronts (SACCF, SB)~~, ~~which is~~ consistent with their more ~~the previous result of~~ frequent occurrence at ~~greater EKE_T of complete CFEs (Figure 5) and their often occurrence at~~ the northern fronts (Table 1). For instance, mean EKE_T at the SAF (4.21 × 10^8 ~~$\mathrm{m^4/s^2}$~~$\mathrm{m^4\ s^{-2}}$) exceeds that at the SB (9.51 × 10^7 $\mathrm{m^4\ s^{-2}}$) by ~~is~~ 3.26 × 10^8 $\mathrm{m^4\ s^{-2}}$~~$\mathrm{m^4/s^2}$ higher than that at SB (9.51 × 10^7 $\mathrm{m^4/s^2}$)~~. During frontal crossing, EKE_T evolution exhibits clear polarity- and direction-dependence. ~~–~~P~~P~~oleward-moving AEs consistently gain kinetic energy during ~~frontal~~ crossing (3.23~~44~~–~~71.76~~88.02% increase), and experience~~with~~ further post-crossing amplification at the three northern fronts (43.52~~14.97~~–71~~88~~.76~~77~~%), indicating sustained energy extraction from the mean flow~~s~~ (Figure 6;~~,~~ Table 2). In contrast, poleward CEs subsequently~~generally~~ lose energy both during and after crossing, ~~at the northern fronts (~~with reductions of ~~i.e., at the NB, SAF, and PF; 3~~31.22–72.74% ~~reduction~~~~16.54–52.24% reduction~~ in the post-crossing phase~~)~~.

Equatorward-moving CFEs exhibit opposing ~~EKE_T~~ behaviors (Figure 7;~~,~~ Table 2).~~:~~ AEs consistently lose energy, showing reductions of 2.59–27.47% ~~reduction~~ during frontal crossing and further decline post-crossing (by 18.41–69.02% ~~reduction~~). In contrast,~~, while~~ CEs generally gain energy, with post-crossing increases of ~~–(~~48.13–

76.70%~~ increase post-crossing~~ at the four ~~–~~northern~~–~~ fronts~~)~~. This pattern reverses at the ~~southern fronts (~~SB~~)~~, where CEs show subsequent~~initial~~ *EKE*$_T$~~ gains during crossing but subsequent~~ losses~~es~~ (e.g., 43.02% decrease after ~~post-SB~~ crossing)~~, mirroring poleward CEs' behavior~~.

These results highlight fundamental asymmetries in eddy-front energy exchange governed by eddy polarity, movement direction, and frontal latitude.

~~The observed polarity asymmetry yields systematically higher post-crossing *EKE*$_T$ for poleward AEs and equatorward CEs, demonstrating a clear polarity- and direction-dependent energy transfer during eddy-jet interactions. While poleward AEs efficiently extract energy from frontal jets, equatorward AEs consistently dissipate energy during and after frontal crossing. Similarly, equatorward CEs gain substantial energy, whereas poleward CEs lose energy at the northern three fronts.~~ They also elucidate the energy compensation observed between frontal-generated partial/transient eddies and complete CFEs (as shown in Figure 5i, j): greater vorticity release to complete CFEs intrinsically reduces local eddy generation. Thus, the energy extraction from frontal jets fuels the complete frontal-crossing equatorward CEs and poleward AEs, contributing to their enhanced post-crossing energetics, consistent with the mesoscale principle of potential vorticity conservation. T~~T~~he anomalous~~ transient~~ energization of equatorward CEs at the~~e SACCF and~~ SB, as well as lower pro-crossing *EKE*$_T$ relative to in-crossing values for poleward AEs, ~~, followed by eventual decay,~~ is likely related~~reflects~~ to the weaker dynamical ~~and~~but stronger hydrographic~~ dynamic~~ characteristics~~s~~ of these~~these~~ southernmost fronts~~s~~ (Park et al., 2019; Thorpe et al., 2002; Vereshchaka et al., 2021).

~~The core findings reported above, including the polarity-based asymmetry in CFE abundance, their long-term EKE intensification, and the direction-selective energy transfers during frontal crossings, are robust to the definition of the frontal zone width. A comprehensive sensitivity analysis, in which the frontal zone half-width was expanded to ±25 km, confirms that all key conclusions remain qualitatively and statistically unchanged (see Supplementary Material, Section S1, Tables S1-S2 and Figs. S3-S6).~~

Table 2. Changes in mean *EKE*$_T$ during different phases for complete cross-frontal eddies (CFEs) relative to pre-crossing values (+: increase; −: decrease). Crossing phases represent when eddies are in the frontal zones, while post-crossing phases indicate when eddies are moving away from the frontal zones. '-' denotes no data.~~lack of SB front poleward-moving CE.~~

Direction	Eddy polarity	Phase	**NB**	**SAF**	**PF**	**SACCF**	**SB**
poleward-moving	AE	crossing	+51.80%	+61.92%	+3.23%	+88.02%	+67.03%
		post	+71.76%	+69.88%	+43.52%	+21.43%	+3.44%
	CE	crossing	−8.44%	−44.63%	−32.58%	−37.68%	-
		post	−31.22%	−72.74%	−57.63%	−69.77%	-
equatorward-moving	AE	crossing	−18.51%	−2.59%	−7.91%	−27.47%	−3.26%
		post	−58.00%	−46.10%	−18.41%	−69.02%	−27.91%
	CE	crossing	+64.28%	+17.91%	+47.86%	+54.70%	−10.89%
		post	+75.78%	+52.33%	+48.13%	+76.70%	−43.02%

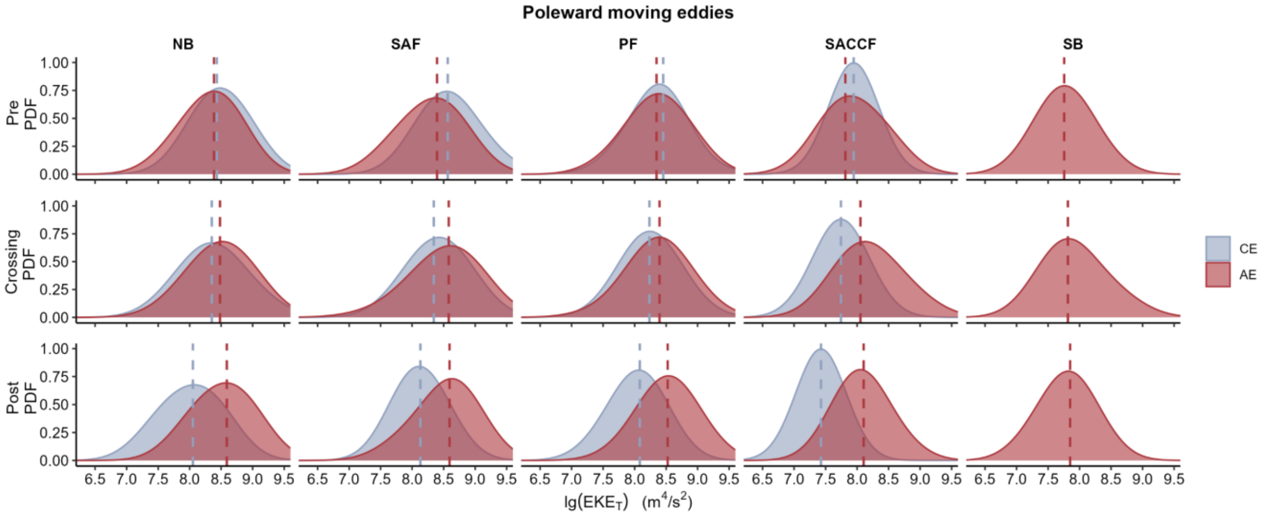

Figure 6. Probability density function (PDF) of EKE_T for poleward-moving CFEs in pre-crossing, crossing, and post-crossing phases. Dashed lines indicate median EKE_T values. Blue and red colors represent CEs and AEs, respectively.

~~Note: The Northern Boundary (NB) is the streamline defining the northern limit of the ACC, following Park et al. (2019).~~

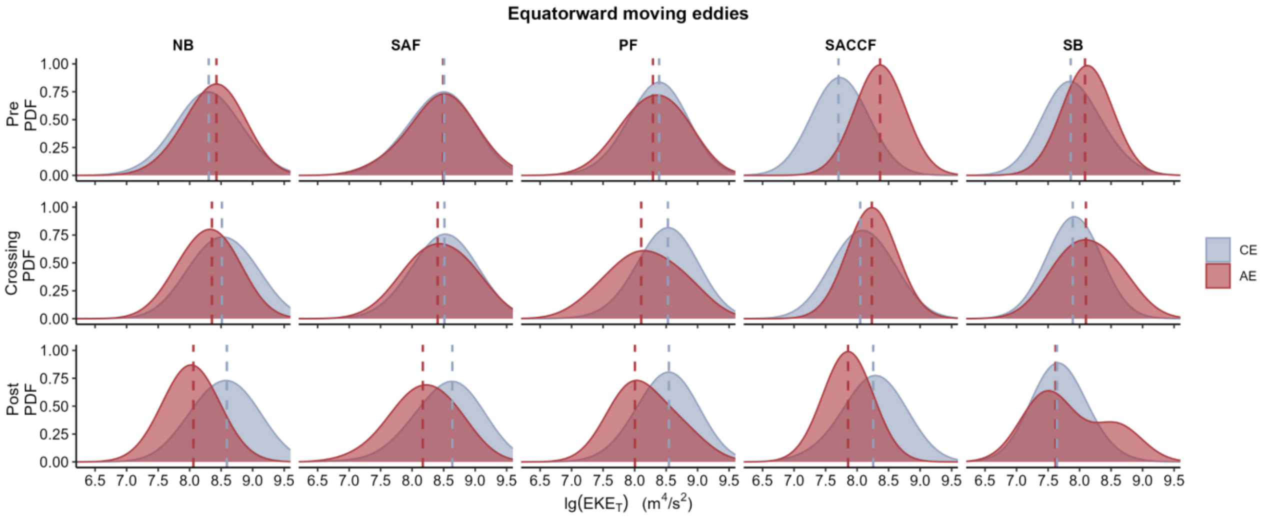

Figure 7. Probability density function (PDF) of EKE_T for equatorward-moving CFEs in pre-crossing, crossing, and post-crossing phases. Dashed lines indicate median EKE_T values. Blue and red colors represent CEs and AEs, respectively.

~~Note: The Northern Boundary (NB) is the streamline defining the northern limit of the ACC, following Park et al. (2019).~~

3.3 Thermohaline transport effects of CFEs

Argo θ-S profiles (Figure 8) reveal that~~ within the same interfrontal zones,~~ cyclonic eddies (CEs) and anticyclonic eddies (AEs) exhibit distinct, polarity-dependent hydrographic signatures within the same interfrontal zones. CEs consistently ~~show~~contain colder, fresher ~~properties~~water with shallower isopycnals (upper 1000 dbar), whereas AEs ~~contain~~are characterized by warmer, saltier water~~s~~ ~~with~~and deeper isopycnals. ~~Argo θ-S profiles (Figure 8) demonstrate that marked meridional thermohaline gradients exist between eddy intervals in different interfrontal zones, with colder and fresher water properties poleward. In the same zones, CEs consistently exhibit colder, fresher properties with shallower isopycnals (upper 1000 dbar), while AEs contain warmer, saltier waters with deeper isopycnals, reflecting their respective meridional origins.~~ These ~~polarity-dependent hydrographies~~contrasts underscore ~~how~~the role of nonlinear eddies in mediating~~e~~ cross-frontal exchange. However~~Nevertheless~~, a subset of ~~some SACCF-PF~~ AEs in the SACCF-PF zone trap~~ped~~ anomalously cold, fresh polar waters ($\theta_{min} = -1.76$°C and $S < 34.0$ psu), similar to ~~the water properties~~those observed in some AEs within~~in~~ the SB-SACCF zone, indicating that AEs can also transport polar waters ~~–~~equatorward~~ transport of polar waters by AEs~~. N~~It’s n~~otably,~~eworthy~~ ~~that~~ eddy-induced vertical motions, upwelling in ~~(~~CEs~~)~~ and downwelling in ~~(~~AEs,~~)~~ ~~achieve~~produce vertical displacements but do not alter θ-S~~isopycnal~~ properties of~~in~~ source water columns (Falkowski et al., 1991; Li et al., 2022). Therefore~~us~~, this mechanism can only ~~explain~~account for~~ some~~ overlapping θ-S signatures~~signatures~~ that arise from~~in~~ vertical~~ly~~ repositioning~~displaced water columns between CEs and AEs~~ of ~~within~~ the same water mass, rather than true cross-frontal modification~~interfrontal zones~~.~~–~~

A~~n a~~nalysis of radius-normalized θ~~ and ~~-S distributions reveals distinct water mass signatures in CEs and AEs across northern interfrontal zones (~~between the~~ SAF-~~ and the northern boundary,~~ NB,~~;~~ ~~between the~~ PF-~~ and ~~SAF,~~;~~ and~~ between the~~ SACCF-~~ and ~~PF). ~~An analysis of radius-normalized θ and S distributions reveals distinct water mass signatures in CEs and AEs across northern interfrontal zones (SAF-NB, PF-SAF, SACCF-PF).~~~~It is important to note that the water mass criteria applied in this study (summarized in Table 3) are primarily representative of the~~

~~Pacific sector of the Southern Ocean, the focus of our work.~~ Core ~~properties of~~ water masses, especially Subantarctic Mode Water (SAMW) and Antarctic Intermediate Water (AAIW), are not circumpolarly uniform but exhibit ~~significant~~substantial regional variability (Bostock et al., 2013; Li et al., 2022). For instance, within the Pacific sector, the salinity minimum of AAIW ranges from ~34.2 in the southeast Pacific formation region to greater than~~>~~ 34.5 in the Tasman Sea after mixing (Bostock et al., 2013).~~;~~ Similarly,~~,~~ ~~and the formation and characteristics of~~ SAMW– ~~also~~ exhibits~~show~~ distinct spatial patterns in its formation and properties (Li et al., 2021). Accordingly~~Therefore~~, the ranges in Table 3 are intended as~~should be interpreted as~~ a practical guide for identifying water masses within the specific Pacific sectoral context of this study.

–Between the ~~In the region between the~~ SAF and ~~the northern boundary (~~NB~~)~~~~In the SAF-NB region~~, well-defined layers of ~~Subantarctic Mode Water (~~SAMW~~)~~, ~~Antarctic Intermediate Water (~~AAIW~~)~~, and Upper Circumpolar Deep Water (UCDW)~~ layers (Table 3)~~ are observed from the upper to lower layer in the AE (Figure 9d, j), confirming their local origin within the Antarctic Convergence Zone. Conversely, the CE in the same ~~region~~zone shows markedly different θ-S~~thermohaline~~ structure~~s~~ (Figure 9a, g), with upper layers (<1000 dbar) lacking SAMW/AAIW signatures and instead containing colder, fresher waters of southern origin. Neutral density (γ^n) surfaces in the CE ~~appear~~are approximately 200~~–300~~ dbar shallower than in the AE, demonstrating that CEs effectively transport high-potential-energy southern waters into the SAF-NB zone. This ~~creates~~establishes strong mesoscale potential energy contrasts between the low-potential-energy waters in AEs and the high-potential-energy waters in CEs, ~~. These contrasts provide~~ an energetic precondition~~basis~~ for baroclinic instability via~~through~~ the release of available potential energy (Fu et al., 2023).

In the PF-SAF region, both the CE and AE maintain thermohaline ~~anomalies~~contrasts similar to those in the SAF-NB zone but with reduced magnitude, preserving the characteristic warmer/saltier AE and colder/fresher CE signatures (the middle panels of Figure 9). Notably, only the CE's upper layer exhibits distinct Winter Water (WW) characteristics, confirming their southern origins. Below this, the normalized CE sequentially displays UCDW and LCDW, while the AE shows only UCDW beneath the relatively warm and salty Antarctic Surface Water within the upper 2000 dbar. The vertical isopycnal structure reveals depth-dependent displacements: in the near-surface layer, the CE's isopycnal γ^n=27.1 kg/m^3 is ~100 dbar shallower than the AE, while at intermediate depths, the CE's isopycnal γ^n=27.6 kg/m^3 (400–600 dbar) is ~500 dbar shallower than the AE (~1000 dbar).

The thermohaline anomalies between CE and AE still exist in the SACCF-PF zone (the right panels of Figure 9). In the CE, a subsurface WW layer overlies a warm UCDW core, with LCDW dominating below 1000 dbar, showing a characteristic of waters south of the SACCF (Aoki et al., 2013; Auger et al., 2021). While the AE also contains these water masses, they show weaker WW expression, a more pronounced $\theta_{\max}$ core, and vertically extended UCDW, reflecting their relatively northern origins. Isopycnals in the CE remain consistently 300–400 dbar shallower than in the AE throughout the water column.

Therefore, the normalized AE and CE possess distinct water mass distributions within the same inter-frontal zones, marked by profound isopycnal thermohaline differences. AEs and CEs transport their respective source water masses into the same~~these~~ zones, amplifying mesoscale hydrographic variability. The above comparative analysis demonstrates that cross-frontal CEs play a dominant role in meridional water mass transport, particularly in the SAF-NB and SACCF-PF zones, consistent with their greater dynamical vigor. This cross-frontal exchange reduces baroclinicity between interfrontal zones while enhancing mesoscale available potential energy within individual zones.

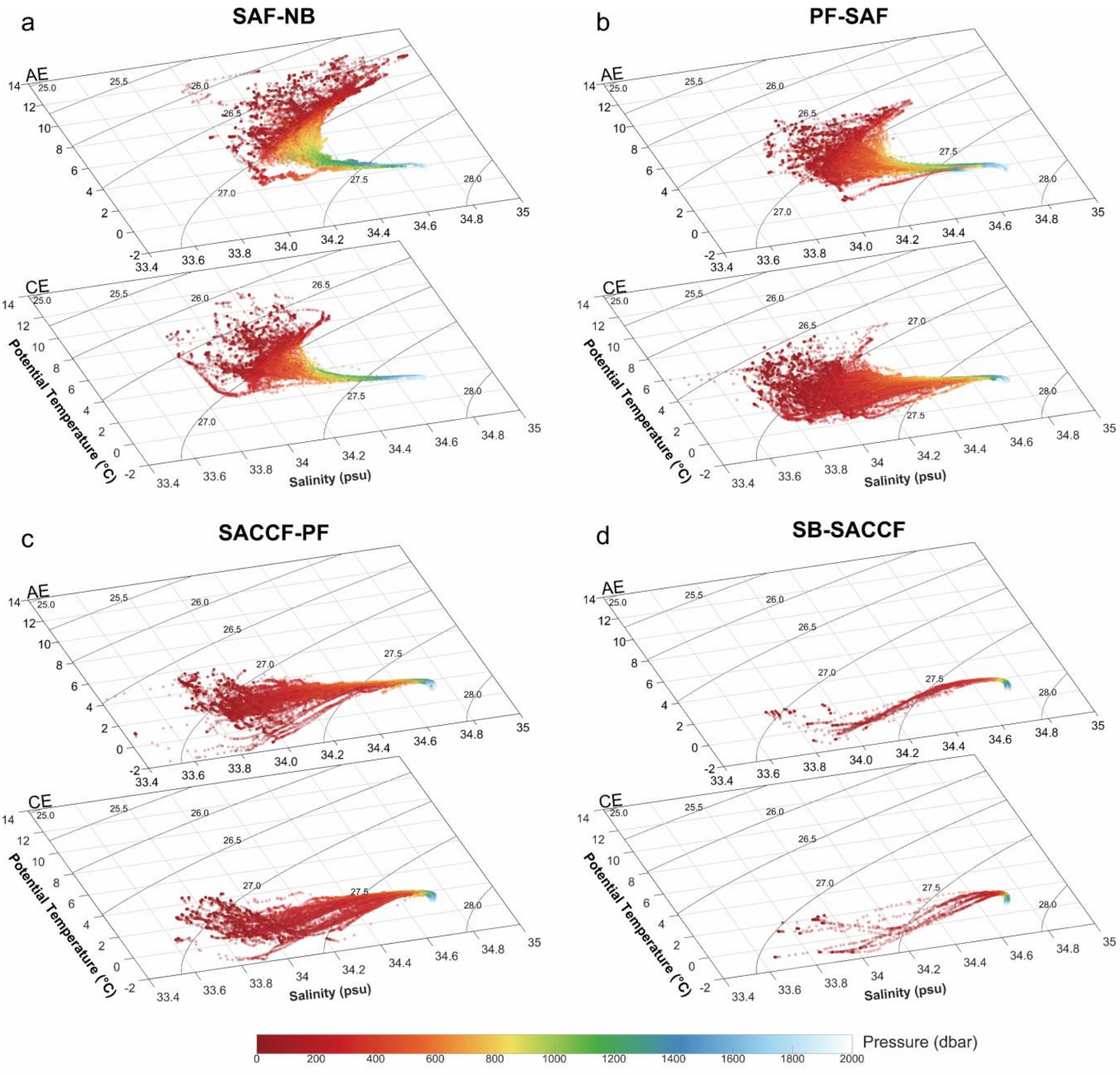

Figure 8. Potential temperature-salinity (θ-S) diagrams in the eddy interiors observed in different inter-frontal zones. (a) SAF-NB; (b) PF-SAF; (c) SACCF-PF; (d) SB-SACCF.

Table 3. Criteria for the division of water masses according to potential temperature (θ, °C), salinity (S, psu) and neutral density (γ^n, kg/m^3). Note: ~~(Note:~~ The ranges listed, particularly for SAMW and AAIW, are primarily representative of the Pacific sector of the Southern Ocean.~~)~~

Water mass	**θ (°C)**	**S (psu)**	**γ^n (kg/m^3)**	**Reference**
SAMW		34.35–34.60	~~26~~27.~~50~~00–27.~~10~~20	Carter et al., 2022; Bostock et al., 2013; Herraiz-Borreguero and Rintoul, 2011 ~~Bostock et al., 2013;~~
AAIW		S_{min} 34.~~15~~28–34.~~30~~40	27.10–27.60	Bostock et al., 2013; Xia et al., 2022; Valla et al., 2018
UCDW	θ_{max}		27.55–28.00	Naveira Garabato et al., 2002
LCDW		S_{max}	28.00–28.2~~6~~7	
WW	θ_{min} < ~~−0.55~~ 2~~3~~.00		~~27.20–27.40~~	~~Azarian et al., 2024; Fischer and Visbeck, 1993~~

*SAMW, Subantarctic Mode Water; AAIW, Antarctic Intermediate Water; UCDW, Upper Circumpolar Deep Water; LCDW, Lower Circumpolar Deep Water; WW, Winter Water.

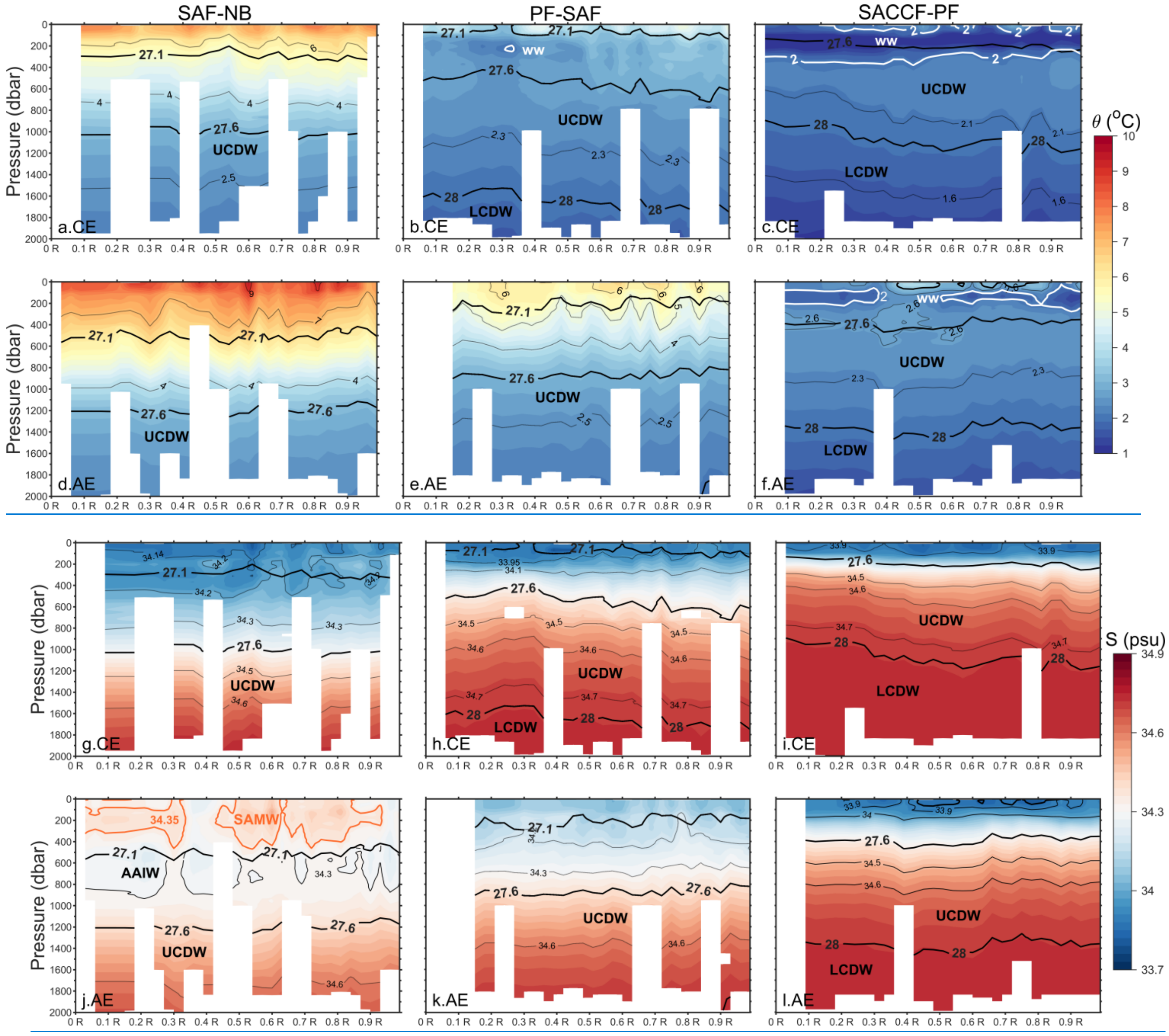
SAF-NB
PF-SAF
SACCF-PF
Pressure (dbar)
a.CE
b.CE
c.CE
d.AE
e.AE
f.AE
g.CE
h.CE
i.CE
j.AE
k.AE
l.AE
0 R 0.1 R 0.2 R 0.3 R 0.4 R 0.5 R 0.6 R 0.7 R 0.8 R 0.9 R
0 200 400 600 800 1000 1200 1400 1600 1800 2000
27.1
27.6
28
UCDW
LCDW
WW
AAIW
SAMW
34.35
θ (°C)
1 2 3 4 5 6 7 8 9 10
S (psu)
33.7 34 34.3 34.6 34.9

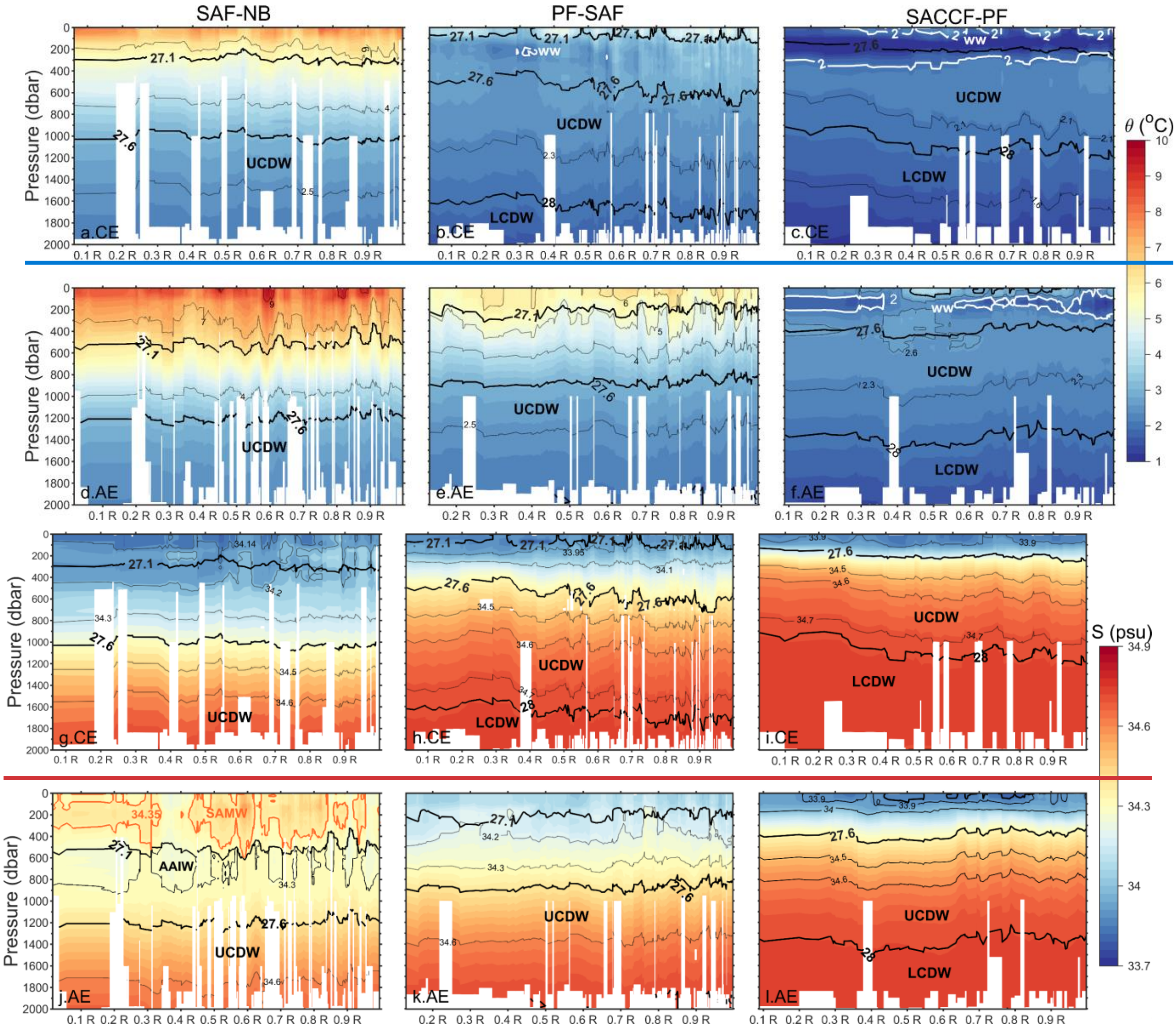

Figure 9. Sectional distributions of *θ* (a–f) and *S* (g–l) along normalized eddy radius (*R*) direction in the inter-frontal zones of SAF-NB (the left panels), PF-SAF (the middle panels), and SACCF-PF (the right panels). Black thick contours indicate neutral density (γ^n, kg/m^3), thin contours represent *θ* or *S* isolines, respectively.

4 Discussion

This study reveals a fundamental polarity- and direction-dependent asymmetry in cross-frontal eddy (CFE)~~s~~ dynamics within the Pacific sector of the SO. This asymmetry manifests in ~~, characterized by~~ three key aspects: (1) a distinct abundance hierarchy among CFE types, (2) contrasting EKE intensities and trends, and (3) polarity- and direction-selective energy transfers during eddy-~~jet~~frontal jet interactions. ~~The equatorward-moving CEs dominate CFE activity (36% of total CFEs), followed by poleward AEs (30%), and then equatorward AEs and poleward CEs. This pattern~~The observed hierarchy,~~,~~ in which CEs predominantly migrate equatorward and AEs poleward, ~~is consistent with~~aligns with established eddy dynamics in the SO (He et al., 2023; Li et al., 2022; Patel et al., 2019). Beyond abundance, t~~T~~he dominant types (equatorward CEs and poleward AEs) exhibit superior energetic characteristics, including~~ with~~ higher EKE levels (Figure~~s~~ 4f~~, S1~~), longer propagation distances (Figure 3), and stronger nonlinearity~~,~~ compared to their counterparts. Our results demonstrate that substantial energy gain during frontal crossing sustains the enhanced energetics of these two dominant complete CFE types, as illustrated in Figure 11. Moreover, the energy compensation relationships (Figure 5i, j) suggest that partial and transient CFEs of the same dominant polarity-direction combinations likely follow a similar energization mechanism. Taken together, these findings indicate that polarity- and direction-dependent eddy-front interactions fundamentally govern CFE energetics and, consequently, their capacity to drive meridional heat and material transport across Southern Ocean frontal zones.

–Although~~Critically, while~~ CFE abundance shows no significant trend over 2000–2022, both polarity groups experienced substantial EKE_T intensification, with CEs gaining energy at (2.27 ± 1.45) × 10^6 $\mathrm{m^4\,s^{-2}\,yr^{-1}}$~~$\mathrm{m^4s^{-2}yr^{-1}}$~~ (excluding the anomalously low 2017 value) and AEs at (2.27 ± 0.94) × 10^6 $\mathrm{m^4\,s^{-2}\,yr^{-1}}$~~$\mathrm{m^4s^{-2}yr^{-1}}$~~. The increasing trends are also robust in terms of annual area-weighted mean EKE ($EKE = EKE_T/S$, where S is the total area of an eddy; Figure S1 in the Supplementary Materials), with trends of 3.71 ± 2.08 $\mathrm{cm^2\,s^{-2}\,yr^{-1}}$ for CEs and 2.58 ± 0.97 $\mathrm{cm^2\,s^{-2}\,yr^{-1}}$ for AEs. The EKE enhancements are even more pronounced for the dominant subsets, equatorward CEs and poleward AEs (Figures 4, S1). These rates substantially exceed previously reported EKE trends. Hogg et al. (2015) estimated a regional mean EKE increase of −14.9 ± 4.1 $\mathrm{cm^2\,s^{-2}\,decade^{-1}}$ under intensifying westerlies in the Pacific sector (1990–2015). Similarly, Zhang et al. (2021) documented an EKE increase of < 20 $\mathrm{cm^2\,s^{-2}\,decade^{-1}}$ south of New Zealand and downstream of the Campbell Plateau, identified as the only region with significant EKE rise in the SO during 1993–2018. The EKE trends for CFEs presented here are considerably larger than these basin-scale estimates. In contrast, non-CFEs exhibit lower EKE levels and no comparable EKE_T increase (Figure 10). The significant area-weighted mean EKE trend for non-frontal crossing CEs is also weaker (Figure S2). These contrasts suggest that the overall *EKE* increase in the Pacific sector is primarily attributable to CFEs. Non-CFEs contribute little to, or may even obscure, the observed *EKE* trends. This finding implies that eddy-front interactions, rather than basin-scale wind forcing alone, may be the primary driver of recent *EKE* trends in the Pacific sector of the SO.

Our results suggest that the e~~This enhancement is primarily driven by equatorward-propagating complete CEs and poleward-propagating complete AEs, contrasting with partial and transient CFEs which show no significant trends (Figures 4, 5). Non-CFEs (both CEs and AEs) also exhibited no comparable *EKE$_T$* or *EKE* trends (Figures 10, S2). This evidence reveals the preference for wind stress driving elevated *EKE* (Hogg et al., 2015; Menna et al., 2020), demonstrating that e~~nhanced wind stress (Hogg et al., 2015; Menna et al., 2020) could preferentially energize~~s~~ cross-frontal activity, especially the CFEs achieving complete frontal crossing (Figure 5). The predominance of equatorward CEs aligns with intensified Ekman transport patterns reported by Shi et al. (2025), also suggesting wind-driven facilitation of meridional eddy migration.

Building on Fu et al.'s (2023) framework of wind-driven energy pathways (baroclinic: mean kinetic energy→ mean available potential energy→mesoscale available potential energy→EKE; barotropic: mean kinetic energy→ EKE), we found that only ~~we demonstrated that cross-frontal eddy-jet interactions exhibit polarity- and direction-dependent energy transfers (as illustrated in Figure 11). e~~Equatorward~~ complete~~ CEs and poleward ~~complete~~ AEs gain~~ substantial~~ kinetic energy from frontal jets (Table 2; Figures 6, 7). This energization likely arises from~~ (e.g., +4852.8633% post-SAF crossing and +6371.8376% post-NB crossing, respectively), potentially through~~ two synergistic mechanisms: (1) barotropic instability from enhanced horizontal shear when eddy rotation aligns with the eastward jet (Qiu et al., 2024), and (2) baroclinic instability triggered by potential energy release for enhanced hydrographic gradients with ambient waters (Fu et al., 2023). ~~These kinetic energy gains during cross-frontal activity dynamically fuel these types of eddies, and subsequently sustain long-distance propagation and meridional heat and material transport (He et al., 2023; Patel et al., 2019; Sun et al., 2019).~~ Conversely, significant energy losses of poleward CEs and equatorward AEs during frontal crossing~~ show significant energy losses (e.g., −59.62% and −29.88% post-SAF crossing)~~, possibly due to counter-rotational turbulent dissipation (Dong et al., 2017; Jan et al., 2017) and upwelling (downwelling)-induced baroclinicity reduction with the ambient waters.

~~The i~~Intensifying and poleward-shifting westerlies have emerged as ~~the~~a dominant dynamic forcing mechanism in the SO (Behrens and Bostock, 2023; Hogg et al., 2015). Meanwhile, buoyancy forcing ~~due to~~from meridionally inhomogeneous ocean warming has been shown~~proved responsible~~ to accelerate the ACC ~~acceleration~~

at 48°S–58°S (Shi et al., 2021). Our results demonstrate~~d~~ that CFEs play a vital role in mediating the oceanic response to these forcings by ~~through~~ compensating for heat transport (Figure 9). By facilitating~~, poleward warm-water transport via AEs and~~ equatorward cold-water transport via CEs and poleward warm-water transport via AEs, CFEs ~~mitigate~~ reduce cross-frontal water mass property gradients. This process~~,~~ effectively buffers~~ing~~ wind- or warming-induced increases in baroclinicity~~ increases~~. thereby~~ This eddy-mediated regulation~~ maintaining~~s~~ the SO's thermal equilibrium and modulating~~es~~ the ACC's response to external forcing. These findings~~,~~ highlight the ~~ing CFEs'~~ dual role of CFEs as both energy transporters and dynamical stabilizers in a changing climate.~~–~~

~~In addition, the multiple-front-crossing eddies warrant attention. These eddies (constituting 5% of total CFEs; Figure 2c–e) demonstrate exceptional transport capacity, achieving significantly farther meridional propagation than their single-front-crossing counterparts (mean 2.16° vs. 0.94°). While the classical paradigm emphasizes rings as the primary cross-jet agents (Dufour et al., 2015), our findings reveal that in frontal convergence zones (e.g., downstream of the Udintsev Fracture Zone), the tight packing of ACC fronts creates a unique environment. Here, robust, coherent vortices—validated to be capable of sustained cross-frontal transport—can interact sequentially with multiple, closely spaced jets during their extended lifetimes. Their extended lifespans and capacity of long-distance propagation (Figure 12) make them highly efficient biogeochemical transporters across fronts. A southward shift in westerlies may push their generation zones poleward (Shi et al. 2025), potentially enhancing their thermal impacts on Antarctic ice shelves through amplified heat delivery.~~

~~In addition, the multiple-front-crossing eddies warrant attention. These eddies (12% of total; Figure 2c–e) demonstrate exceptional transport capacity, with apparently farther meridional propagation than single-front-crossing eddies (mean 2.24° vs. 0.78°). Their extended lifespans and capacity of long-distance propagation (Figure 12) make them highly efficient biogeochemical transporters across fronts. A southward shift in westerlies may push their generation zones poleward (Shi et al. 2025), potentially enhancing their thermal impacts on Antarctic ice shelves through amplified heat delivery.~~

~~It should be noted that this study defines each frontal zone as a 30 km-wide strip-shaped area but does not account for potential interannual or seasonal variations that may extend beyond this range. Similarly, all qualified Argo profiles from 2000 to 2022 were used without considering interannual or seasonal variability in hydrographic properties. These limitations inevitably introduce certain uncertainties.~~

This study has several limitations that should be noted. First, the analysis does not account for potential interannual or seasonal variations in frontal positions~~It should be noted that this study does not account for potential~~

~~interannual or seasonal variations of the fronts that may extend beyond the adopted frontal range~~. However, a comprehensive sensitivity analysis, in which the frontal zone half-width was expanded to ±(25+*R*) km, confirms that all key conclusions remain qualitatively and statistically robust (see Supplementary Materials, Tables S1 and S2, and Figures S3–S6). Second~~imilarly~~, the hydrographic analysis utilized all qualified Argo profiles from 2000 to 2022~~2 were used~~ without segregating~~considering~~ interannual or seasonal variability, which may introduce some uncertainty into the normalized water mass properties. Finally, while this study focuses on eddy characteristics, it does not evaluate the dynamic properties of the frontal jets themselves. A detailed analysis of jet variability and energy transfer is essential for a more comprehensive mechanistic understanding of eddy-jet interactions and represents an important direction for future research. ~~in hydrographic properties. These limitations inevitably introduce certain uncertainties.~~

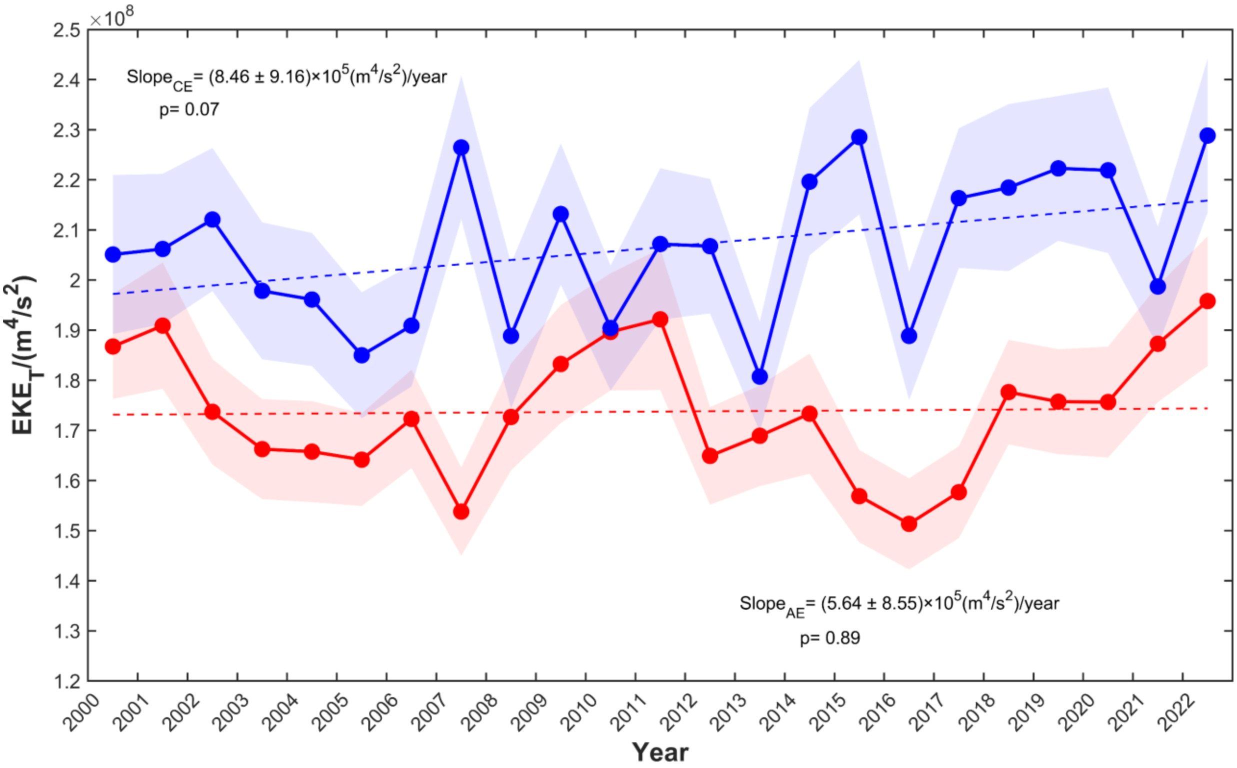

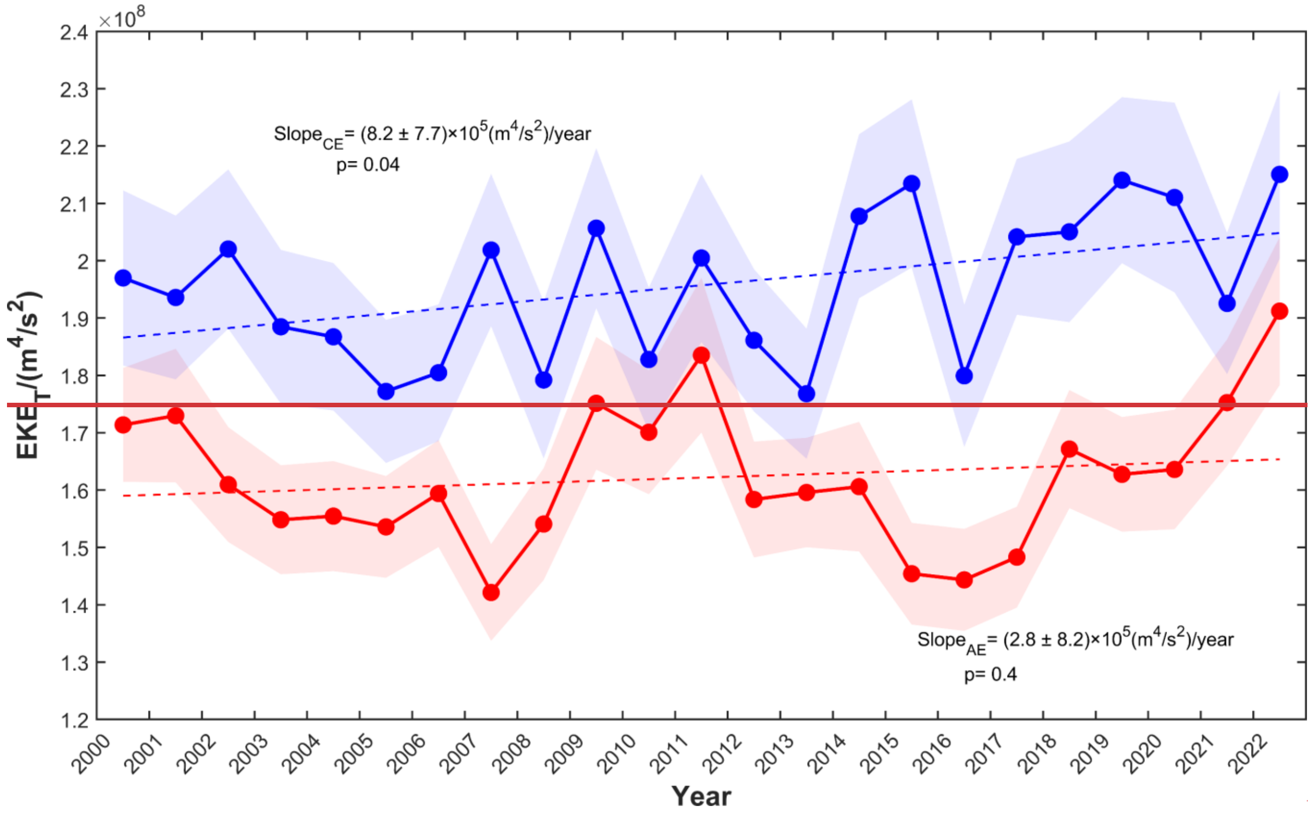

Figure 10. Time series of annual mean *EKE_T* for eddies in the interfrontal zones. *EKE_T* is shown by blue solid line for CEs and red solid line for AEs, with linear regression indicated by dashed lines, error shadings representing one standard deviation, and slope values given with ± 95% confidence intervals.

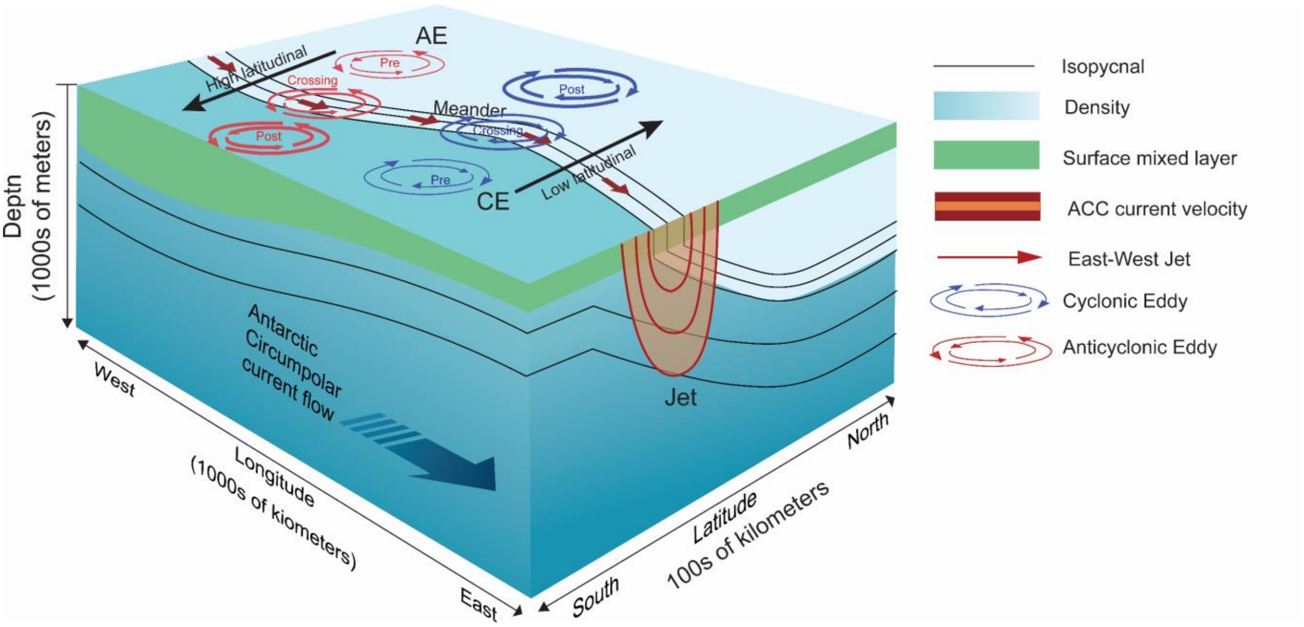

Figure 11. Illustrations of EKE variations during frontal crossing for poleward AEs and equatorward CEs (modified from Figure 1 in Chapman et al., 2020). The thickness of rotational velocity vectors represents relative flow intensity.

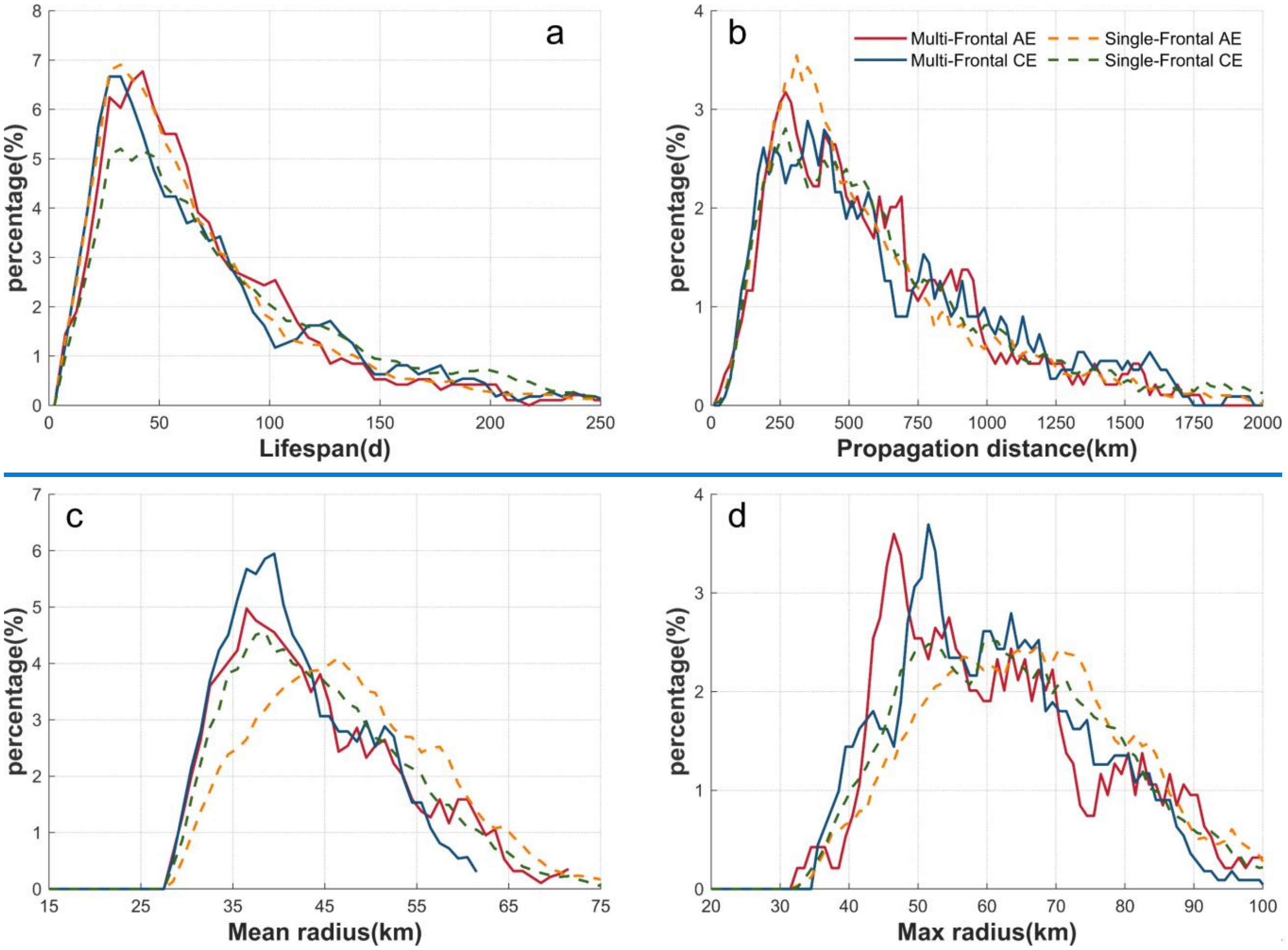

~~**Figure 12. Proportional distributions lifespan (a), propagation distance (b), mean radius (c) and max radius (d) for multi-front-crossing eddies (solid lines) versus single-front-crossing eddies (dashed lines).**~~

5 Conclusions

This study provides a comprehensive characterization~~reveals a fundamental polarity- and direction-dependent asymmetry in the behavior~~ of cross-frontal eddies (CFEs) in the ~~SO's~~ Pacific sector of the Southern Ocean, revealing fundamental asymmetries that govern their role in meridional transport and energy exchange. Through the integration of multi-decadal satellite altimetry and in-situ hydrographic data, we have demonstrated that CFE activity is not random but follows a well-defined polarity- and direction-dependent~~with primary implications for heat transport and climate regulation. A clear~~ hierarchy. The predominance of~~exists that~~ equatorward-moving cyclonic eddies (CEs) ~~are the most prevalent~~ and ~~energetic (36% of total CFEs), followed by~~ poleward-moving anticyclonic eddies (AEs) reflects an intrinsic organization in cross-frontal exchange pathways that has profound implications for Southern Ocean dynamics~~(30%)~~.

Three key findings emerge from our analysis. First, the observed CFE abundance hierarchy is complemented by significant differences in energetic characteristics, with the dominant types (equatorward CEs and poleward AEs) exhibiting superior kinetic energy levels, longer propagation distances, and stronger nonlinearity. Second, these eddies experience sustained energization through polarity-selective energy transfers during frontal crossings, gaining kinetic energy from the eastward frontal jets while their counterparts experience energy dissipation. The intensification of CFE activity has occurred over the past two decades, with *EKE* trends substantially exceeding previous basin-scale estimates, suggesting that eddy-front interactions, rather than wind forcing alone, drive recent energetic changes in the region. Third, hydrographic analyses confirm that CFEs function as effective transporters of distinct water masses, with CEs and AEs maintaining sharp thermohaline contrasts within the same interfrontal zones. This cross-frontal exchange reduces large-scale baroclinicity while enhancing mesoscale available potential energy, creating a dynamic balance that regulates meridional heat transport.

~~The compensatory transport mechanism identified, whereby equatorward cold-water transport by CEs balances poleward warm-water transport by AEs, reveals CFEs' crucial role as dynamical stabilizers in the~~

~~Southern Ocean system.~~ As climate change intensifies westerly winds and modifies buoyancy forcing, CFEs are likely to play an increasingly important role in modulating the ACC's response to external forcing. Their ability to maintain thermal equilibrium across frontal zones highlights their significance for understanding future changes in Southern Ocean circulation, carbon uptake, and global climate feedbacks. Future research should focus on quantifying the precise contribution of CFEs to meridional heat and carbon fluxes and investigating how their stabilizing role might evolve under continued climate change.

~~These two types dominate long-distance cross-frontal transport and have significantly intensified over the past two decades (2000–2022), gaining kinetic energy from the frontal jets during crossing. This trend is absent in eddies that partially or transiently cross fronts, or do not cross fronts, showing that wind stress intensification preferentially energizes complete cross-frontal activity. A dual mechanism could explain the energy gains in the equatorward CEs and poleward AEs that (1) barotropic instability from enhanced horizontal shear due to aligned rotation with eastward jets and (2) baroclinic instability from the potential energy release created by sharp hydrographic contrasts with surrounding waters. Conversely, counter-rotational eddies experience eddy dissipation. CFEs act as efficient transporters of distinct water masses: CEs trap and carry cold, fresh southern waters equatorward, while AEs transport warm, salty northern waters poleward. This process directly mitigates reduces the sharp meridional gradients. By compensating for wind-driven increases and inhomogeneous ocean warming in baroclinicity, CFEs help maintain the SO's thermal equilibrium and modulate the ACC's response to climate change.~~

~~These results advance our understanding of cross-frontal mesoscale processes in the ACC and potentially provide a mechanism-based explanation of the distribution of marine species in the SO, which originate from the regions beyond the Antarctic region. The identified polarity asymmetries and preference for energy transfers have vital implications for parameterizing eddy effects in climate models, particularly under projected wind regime shifts.~~

~~The core findings reported above, including the polarity-based asymmetry in CFE abundance, their long-term EKE intensification, and the direction-selective energy transfers during frontal crossings, are robust to the definition of the frontal zone width. A comprehensive sensitivity analysis, in which the frontal zone half-width was expanded to ±25 km, confirms that all key conclusions remain qualitatively and statistically unchanged (see Supplementary Material, Section S1, Tables S1-S2 and Figs. S3-S6).~~

Data availability

The satellite altimeter data are available online at the Copernicus Marine Service (the CMEMS all-satellite L4 SLA product~~Global Ocean Gridded L4 Sea Surface Heights And Derived Variables~~ at https://doi.org/10.48670/moi-00148~~https://marine.copernicus.eu/~~). The data were accessed and downloaded on 18th December, 2025. The frontal data used in this study were sourced from Park et al. (2019) at https://doi.org/10.17882/59800. Argo profiles are available at the website of https://argo.ucsd.edu/data/~~http://www.argo.net~~.

Author contributions

Huimin Wang: Methodology, Software, Formal analysis, Investigation, Data curation, Writing-original draft, Visualization. Lingqiao Cheng: Conceptualization, Methodology, Resources, Writing-original draft, Writing-review & editing, Supervision, Project administration, Funding acquisition. Erik Behrens: Validation, Writing-review & editing. Zhuang Chen: Validation, Writing-review & editing. Jennifer Devine: Writing-review & editing. Guoping Zhu: Resources, Writing-review & editing, Funding acquisition.

Competing Interests

The authors declare that they have no conflict of interest.

Acknowledgments

We thank the Key Laboratory of Sustainable Exploitation of Oceanic Fisheries Resources, Shanghai Ocean University and the Joint Research Center on Antarctic Marine Science supported by Shanghai Ocean University, Earth Sciences New Zealand, and the University of Otago for their support and the utilization of their laboratory facilities.

Financial support

This work was funded by the National Key Research and Development Program of China (grant no. 2023YFE0104500), the National Natural Science Foundation of China (grant no. 42130402), Shanghai Top-tier Talent Program of Eastern Talent Plan (grant no. BJKJ2024059), and supported by the Catalyst Fund from Government funding, administered by the Royal Society Te Apārangi.

References

Aoki, S., Kitade, Y., Shimada, K., Ohshima, K. I., Tamura, T., Bajish, C. C., Moteki, M., and Rintoul, S. R.: Widespread freshening in the Seasonal Ice Zone near 140°E off the Adélie Land Coast, Antarctica, from 1994 to 2012. J. Geophys. Res. Oceans., 118(11), 6046–6063, https://doi.org/10.1002/2013JC009009, ~~2020~~2013.

Auger, M., Morrow, R., Kestenare, E., Sallée, J.-B., and Cowley, R.: Southern Ocean in-situ temperature trends over 25 years emerge from interannual variability. Nat. Commun., 12(1), 1840, https://doi.org/10.1038/s41467-020-20781-1, 2021.

~~Azarian, C., Bopp, L., Sallée, J.-B., Swart, S., Guinet, C., and d'Ovidio, F.: Marine heatwaves and global warming impacts on winter waters in the Southern Indian Ocean. J. Mar. Syst., 243, 103962, https://doi.org/10.1016/j.jmarsys.2023.103962, 2024.~~

Barthel, A., McC. Hogg, A., Waterman, S., and Keating, S.: Jet–Topography Interactions Affect Energy Pathways to the Deep Southern Ocean. J. Phys. Oceanogr., 47(7), 1799-1816, https://doi.org/10.1175/JPO-D-16-0220.1, 2017.

Behrens, E., and Bostock, H.: The Response of the Subtropical Front to Changes in the Southern Hemisphere Westerly Winds—Evidence From Models and Observations. J. Geophys. Res. Oceans., 128(2), e2022JC019139, https://doi.org/10.1029/2022JC019139, 2023.

Belkin, I. M., and Gordon, A. L.: Southern Ocean fronts from the Greenwich meridian to Tasmania, J. Geophys. Res., 101, 3675-3696, https://doi.org/10.1029/95JC02750, 1996.

Bostock, H. C., Sutton, P. J., Williams, M. J., and Opdyke, B. N.: Reviewing the circulation and mixing of Antarctic Intermediate Water in the South Pacific using evidence from geochemical tracers and Argo float trajectories, Deep Sea Research Part I: Oceanographic Research Papers, 73, 84–98, doi:10.1016/j.dsr.2012.11.007, 2013.

Carter, L., Bostock-Lyman, H., and Bowen, M.: Water masses, circulation and change in the modern Southern Ocean, in: Antarctic Climate Evolution (Second Edition), edited by: Florindo, F., Siegert, M., De Santis, L., and Naish, T., Elsevier, Amsterdam, 165–197, https://doi.org/10.1016/B978-0-12-819109-5.00003-7, 2022.

Chapman, C., and Sallée, J.-B.: Isopycnal Mixing Suppression by the Antarctic Circumpolar Current and the Southern Ocean Meridional Overturning Circulation. J. Phys. Oceanogr., 47(8), 2023–2045, https://doi.org/10.1175/JPO-D-16-0263.1, 2017.

Chapman, C. C., Lea, M.-A., Meyer, A., Sallée, J.-B., and Hindell, M.: Defining Southern Ocean fronts and their influence on biological and physical processes in a changing climate, Nat. Clim. Change., 10(3), 209–219, https://doi.org/10.1038/s41558-020-0705-4, 2020.

Chelton, D. B., Schlax, M. G., and Samelson, R. M.: Global observations of nonlinear mesoscale eddies, Prog. Oceanogr., 91(2), 167–216, https://doi.org/10.1016/j.pocean.2011.01.002, 2011.

Copernicus Marine Service: Global Ocean Gridded L4 Sea Surface Heights And Derived Variables Reprocessed 1993 Ongoing (SEALEVEL_GLO_PHY_L4_MY_008_047), Mercator Ocean International [data set], https://doi.org/10.48670/moi-00148, 2024.

De Szoeke, R. A. and Levine, M. D.: The advective flux of heat by mean geostrophic motions in the Southern Ocean, Deep-Sea Res. Part A Oceanogr. Res. Pap., 28(10), 1057–1085, https://doi.org/10.1016/0198-0149(81)90048-0, 1981.

~~Deacon, G. E. R.: The hydrology of the southern ocean, Discovery Rep., 15, Cambridge University Press, Cambridge, 124pp., 1937.~~

Dong, D., Brandt, P., Chang, P., Schütte, F., Yang, X., Yan, J., and Zeng, J.: Mesoscale eddies in the northwestern Pacific Ocean: three-dimensional eddy structures and heat/salt transports, J. Geophys. Res. Oceans., 122, 9795~~–~~–9813, https://doi.org/10.1002/2017JC013303, 2017.

Duan, Y., Liu, H., Yu, W., and Hou, Y.: Eddy properties in the Pacific sector of the Southern Ocean from satellite altimetry data, Acta Oceanol. Sin., 35, 28~~–~~–34, https://doi.org/10.1007/s13131-016-0946-2, 2016.

Duan, M., Ashford, J. R., Bestley, S., Wei, X. Y., Walters, A., and Zhu, G. P.: Otolith chemistry of Electrona antarctica suggests a potential population marker distinguishing the southern Kerguelen Plateau from the eastward-flowing Antarctic Circumpolar Current, Limnol. Oceanogr., 62(2), 405~~–~~–421, https://doi.org/10.1002/lno.11612, 2020.

Falkowski, P. G., Ziemann, D., Kolber, Z., and Bienfang, P. K.: Role of eddy pumping in enhancing primary production in the ocean, Nature., 352, 55~~–~~–58, https://doi.org/10.1038/352055a0, 1991.

~~Fischer, J. and Visbeck, M.: Deep velocity profiling with self-contained ADCPs, J. Atmos. Ocean. Tech., 10(5), 764–773, https://doi.org/10.1175/1520-0426(1993)010<0764:DVPWSC>2.0.CO;2, 1993.~~

Foppert, A., Donohue, K. A., Watts, D. R., and Tracey, K. L.: Eddy heat flux across the Antarctic Circumpolar Current estimated from sea surface height standard deviation, J. Geophys. Res. Oceans., 122(8), 6947~~–~~–6964, https://doi.org/10.1002/2017JC012837, 2017.

Frenger, I., Münnich, M., Gruber, N., and Knutti, R.: Southern Ocean eddy phenomenology, J. Geophys. Res. Oceans., 120(11), 7413~~–~~–7449, https://doi.org/10.1002/2015JC011047, 2015.

Fu, G., Yang, Y., Liang, X. S., and Zhao, Y.: Characteristics and dynamics of the interannual eddy kinetic energy variation in the central Pacific sector of the Southern Ocean, J. Geophys. Res. Oceans., 128, e2022JC019618, https://doi.org/10.1029/2022JC019618, 2023.

Gille, S. T.: Mean sea surface height of the Antarctic Circumpolar Current from Geosat data: method and application, J. Geophys. Res. Oceans., 99(C9), 18255~~–~~–18273, https://doi.org/10.1029/94JC01172, 1994.

Hallberg, R., and Gnanadesikan, A.~~–~~: An Exploration of the Role of Transient Eddies in Determining the Transport of a Zonally Reentrant Current, J. Phys. Oceanogr., 31, 3312–~~–~~3330. https://doi.org/10.1175/1520-0485(2001)031%3C3312:AEOTRO%3E2.0.CO;2, 2001.

Hallberg, R., and Gnanadesikan, A.: The Role of Eddies in Determining the Structure and Response of the Wind-Driven Southern Hemisphere Overturning: Results from the Modeling Eddies in the Southern Ocean (MESO) Project, J. Phys. Oceanogr., 36(12), 2232–~~–~~2252, https://doi.org/10.1175/JPO2980.1, 2006.

He, Q., Zhan, W., Cai, S., Du, Y., Chen, Z., Tang, S., and Zhan, H.: Enhancing impacts of mesoscale eddies on Southern Ocean temperature variability and extremes, Proc. Natl. Acad. Sci. U.S.A., 120, e2302292120, https://doi.org/10.1073/pnas.2302292120, 2023.

Henson, S. A. and Thomas, A. C.: A census of oceanic anticyclonic eddies in the Gulf of Alaska, Deep-Sea Res. Part. I., 55, 163–176, https://doi.org/10.1016/j.dsr.2007.11.005, 2008.

Herraiz-Borreguero, L. and Rintoul, S. R.: Subantarctic mode water: distribution and circulation, Ocean Dynamics, 61, 103–126, doi:10.1007/s10236-010-0352-9, 2011.

Hogg, A. M., Meredith, M. P., Chambers, D. P., Abrahamsen, E. P., Hughes, C. W., and Morrison, A. K.: Recent trends in the Southern Ocean eddy field, J. Geophys. Res. Oceans., 120, 257–267, https://doi.org/10.1002/2014JC010470, 2015.

Holte, J. W., Talley, L. D., Chereskin, T. K., and Sloyan, B. M.: Subantarctic mode water in the southeast Pacific: effect of exchange across the Subantarctic Front, J. Geophys. Res. Oceans., 118, 2052~~–~~–2066, https://doi.org/10.1002/jgrc.20144, 2013.

Hughes, C. W.: Rossby waves in the Southern Ocean: a comparison of TOPEX/POSEIDON altimetry with model predictions, J. Geophys. Res. Oceans., 100, 15933~~–~~–15950, https://doi.org/10.1029/95JC01380, 1995.

Hughes, C. W. and Ash, E. R.: Eddy forcing of the mean flow in the Southern Ocean, J. Geophys. Res. Oceans., 106, 2713~~-~~–2722, https://doi.org/10.1029/2000JC900332, 2001.

Isern-Fontanet, J., García-Ladona, E., and Font, J.: Vortices of the Mediterranean Sea: an altimetric perspective, J. Phys. Oceanogr., 36, 87~~–~~–103, https://doi.org/10.1175/JPO2826.1, 2006.

Jan, S., Mensah, V., Andres, M., Chang, M.-H., and Yang, Y. J.: Eddy–Kuroshio interactions: local and remote effects, J. Geophys. Res. Oceans., 122, 9744~~–~~–9764, https://doi.org/10.1002/2017JC013476, 2017.

Kim, Y. S. and Orsi, A. H.: On the variability of Antarctic Circumpolar Current fronts inferred from 1992–2011 altimetry, J. Phys. Oceanogr., 44, 3054~~–~~–3071, https://doi.org/10.1175/JPO-D-13-0217.1, 2014.

Li, Z., England, M. H., Groeskamp, S., Cerovečki, I., and Luo, Y.: The Origin and Fate of Subantarctic Mode Water in the Southern Ocean, J. Phys. Oceanogr.,~~Journal of Physical Oceanography,~~ 51(9), 2951–2972, doi:10.1175/JPO-D-20-0174.1, 2021.

Li, Z., Groeskamp, S., Cerovečki, I., and England, M. H.: The origin and fate of Antarctic Intermediate Water in the Southern Ocean, J. Phys. Oceanogr., 52, 2873~~–~~–2890, https://doi.org/10.1175/JPO-D-21-0221.1, 2022.

Matsuoka, D., Araki, F., Inoue, Y., and Sasaki, H.: A new approach to ocean eddy detection, tracking, and event visualization – application to the northwest Pacific Ocean, Procedia Comput. Sci., 80, 1601~~–~~–1611, https://doi.org/10.1016/j.procs.2016.05.491, 2016.

Menna, M., Cotroneo, Y., Falco, P., Zambianchi, E., Di Lemma, R., Poulain, P.-M., Fusco, G., and Budillon, G.: Response of the Pacific sector of the Southern Ocean to wind stress variability from 1995 to 2017, J. Geophys. Res. Oceans., 125, e2019JC015696, https://doi.org/10.1029/2019JC015696, 2020.

~~Meredith, M. P. and Hogg, A. M.: Circumpolar response of Southern Ocean eddy activity to a change in the Southern Annular Mode, Geophys. Res. Lett., 33, L16608, https://doi.org/10.1029/2006GL026499, 2006.~~

Moreau, S., Della Penna, A., Llort, J., Patel, R., Langlais, C., Boyd, P. W., Matear, R. J., Phillips, H. E., Trull, T. W., Tilbrook, B., Lenton, A., and Strutton, P. G.: Eddy-induced carbon transport across the Antarctic Circumpolar Current, Glob. Biogeochem. Cycles., 31, 1368~~–~~–1386, https://doi.org/10.1002/2017GB005669, 2017.

Morrow, R., Church, J., Coleman, R., Chelton, D., and White, N.: Eddy momentum flux and its contribution to the Southern Ocean momentum balance, Nature., 357, 482~~–~~–484, https://doi.org/10.1038/357482a0, 1992.

Morrow, R., Coleman, R., Church, J., and Chelton, D.: Surface eddy momentum flux and velocity variances in the Southern Ocean from Geosat altimetry, J. Phys. Oceanogr., 24, 2050~~–~~–2071, https://doi.org/10.1175/1520-0485(1994)024<2050:SEMFAV>2.0.CO;2 1994.

Morrow, R., Ward, M. L., Hogg, A. M., and Pasquet, S.: Eddy response to Southern Ocean climate modes, J. Geophys. Res. Oceans., 115, C10030, https://doi.org/10.1029/2009JC005894, 2010.

~~Mulet, S., Rio, M. H., Mignot, A., Guinehut, S., and Morrow, R.: A new estimate of the global 3-D geostrophic ocean circulation based on satellite data and in-situ measurements, Deep Sea Res. Part II., 77–80, 70–81, https://doi.org/10.1016/j.dsr2.2012.04.012, 2012.~~

Naveira Garabato, A. C., Ferrari, R., and Polzin, K. L.: Eddy stirring in the Southern Ocean, J. Geophys. Res., 116, C09017, https://doi.org/10.1029/2010JC006818, 2011.

Naveira Garabato, A. C., Heywood, K. J., and Stevens, D. P.: Modification and pathways of Southern Ocean Deep Waters in the Scotia Sea, Deep-Sea Res. Part I., 49, 681–705, https://doi.org/10.1016/S0967-0637(01)00071-1, 2002.

Okubo, A.: Horizontal dispersion of floatable particles in the vicinity of velocity singularities such as convergences, Deep-Sea Res. Oceanogr. Abstr., 17, 445–454, https://doi.org/10.1016/0011-7471(70)90059-8, 1970.

Orsi, A. H., Whitworth, T., and Nowlin, W. D.: On the meridional extent and fronts of the Antarctic Circumpolar Current, Deep-Sea Res. Part I., 42, 641–673, https://doi.org/10.1016/0967-0637(95)00021-W, 1995.

Park, Y.-H., Gamberoni, L., and Charriaud, E.: Frontal structure, water masses, and circulation in the Crozet Basin, J. Geophys. Res., 98, 12361–12385, https://doi.org/10.1029/93JC00938, 1993.

Park, Y.-H., Park, T., Kim, T.-W., Lee, S.-H., Hong, C.-S., Lee, J.-H., Rio, M.-H., Pujol, M.-I., Ballarotta, M., Durand, I., and Provost, C.: Observations of the Antarctic Circumpolar Current over the Udintsev Fracture Zone, the narrowest choke point in the Southern Ocean, J. Geophys. Res. Oceans., 124, 4511–4528, https://doi.org/10.1029/2019JC015024, 2019.

Patel, R. S., Phillips, H. E., Strutton, P. G., Lenton, A., and Llort, J.: Meridional heat and salt transport across the Subantarctic Front by cold-core eddies, J. Geophys. Res. Oceans., 124, 981–1004, https://doi.org/10.1029/2018JC014655, 2019.

Pujol, M.-I. and Grassi, K.: Product user manual for sea level altimeter products: SEALEVEL_GLO_PHY_L4_NRT_008_046, SEALEVEL_EUR_PHY_L4_NRT_008_060, SEALEVEL_GLO_PHY_L4_MY_008_067, SEALEVEL_EUR_PHY_L4_MY_008_068, Issue 1.0, Copernicus Marine Environment Monitoring Service (CMEMS), https://catalogue.marine.copernicus.eu/documents/PUM/CMEMS-SL-PUM-008-046-047-060-068.pdf, 2025.

~~Pujol, M. I., and Grassi, K. (2025). *Product user manual for sea level altimeter products: SEALEVEL_GLO_PHY_L4_NRT_008_046, SEALEVEL_EUR_PHY_L4_NRT_008_060, SEALEVEL_GLO_PHY_L4_MY_008_067, SEALEVEL_EUR_PHY_L4_MY_008_068* (Issue 1.0). Copernicus Marine Environment Monitoring Service (CMEMS). https://catalogue.marine.copernicus.eu/documents/PUM/CMEMS-SL-PUM-008-046-047-060-068.pdf~~

Qiu, C., Yang, Z., Feng, M., Yang, J., Rippeth, T. P., Shang, X., Sun, Z., Jing, C., and Wang, D.: Observational energy transfers of a spiral cold filament within an anticyclonic eddy, Prog. Oceanogr., 220, 103187, https://doi.org/10.1016/j.pocean.2023.103187, 2024.

Sallée, J.-B., Speer, K., and Morrow, R.: Southern Ocean fronts and their variability to climate modes, J. Climate., 21, 3020–3039, 2008.

Saunders, R. A., Collins, M. A., Stowasser, G., and Tarling, G. A.: Southern Ocean mesopelagic fish communities in the Scotia Sea are sustained by mass immigration, Mar. Ecol. Prog. Ser., 569, 173–185, https://doi.org/10.3354/meps12093, 2017.

-Saraceno, M. and Provost, C.: On eddy polarity distribution in the southwestern Atlantic, Deep Sea Research Part I: Oceanographic Research Papers, 69, 62–69, doi:10.1016/j.dsr.2012.07.001, 2012.

Shi, F., Shi, Q., Luo, Y. Y., Wu, R. H., Yang, Q. H., Liu, J. P., Yang, J., and Song, J.: Meridional shift of Southern Ocean mesoscale eddies since the 1990s, Adv. Atmos. Sci., 42, 1–10, https://doi.org/10.1007/s00376-024-4249-9, 2025.

Shi, J. R., Talley, L. D., Xie, S. P., Peng, Q., and Liu, W.: Ocean warming and accelerating Southern Ocean zonal flow, Nat. Clim. Chang., 11, 1090—1097, https://doi.org/10.1038/s41558-021-01212-5, 2021.

Sokolov, S. and Rintoul, S. R.: Structure of Southern Ocean fronts at 140°E, J. Mar. Syst., 37, 151–184, https://doi.org/10.1016/S0924-7963(02)00200-2, 2002.

Sokolov, S. and Rintoul, S. R.: On the relationship between fronts of the Antarctic Circumpolar Current and surface chlorophyll concentrations in the Southern Ocean, J. Geophys. Res. Oceans., 112, C07030, https://doi.org/10.1029/2006JC004072, 2007.

~~Speer, K., Rintoul, S. R., and Sloyan, B.: The Diabatic Deacon Cell, J. Phys. Oceanogr., 30, 3212–3222,~~

~~https://doi.org/10.1175/1520-0485(2000)030<3212:TDDC>2.0.CO;2, 2000.~~

Sprintall, J.: Seasonal to interannual upper-ocean variability in the Drake Passage, J. Mar. Res., 61, 27–57, https://doi.org/10.1357/002224003321586408, 2003.

Straub, D. N.: On the transport and angular momentum balance of channel models of the Antarctic Circumpolar Current, J. Phys. Oceanogr., 23, 776–782, https://doi.org/10.1175/1520-0485(1993)023<0776:OTTAAM>2.0.CO;2, 1993.

~~Sun, B., Liu, C., and Wang, F.: Global meridional eddy heat transport inferred from Argo and altimetry observations, Sci. Rep., 9, 1345, https://doi.org/10.1038/s41598-018-38069-2, 2019.~~

Swart, N. C., Ansorge, I. J., and Lutjeharms, J. R. E.: Detailed characterization of a cold Antarctic eddy, J. Geophys. Res. Oceans., 113, C01009, https://doi.org/10.1029/2007JC004190, 2008.

Thompson, A. F., Haynes, P. H., Wilson, C., and Richards, K. J.: Rapid Southern Ocean front transitions in an eddy-resolving ocean GCM, Geophys. Res. Lett., 37, L23602, https://doi.org/10.1029/2010GL045386, 2010.

Thompson, A. F. and Sallée, J.-B.: Jets and topography: Jet transitions and the impact on transport in the Antarctic Circumpolar Current, J. Phys. Oceanogr., 42, 956–972, https://doi.org/10.1175/JPO-D-11-0135.1, 2012.

Thorpe, S. E., Heywood, K. J., Brandon, M. A., and Stevens, D. P.: Variability of the southern Antarctic Circumpolar Current front north of South Georgia, J. Mar. Syst., 37, 87–105, https://doi.org/10.1016/S0924-7963(02)00197-5, 2002.

Valla, D., Piola, A. R., Meinen, C. S., and Campos, E.: Strong mixing and recirculation in the northwestern Argentine Basin, J. Geophys. Res. Oceans., 123, 4624–4648, https://doi.org/10.1029/2018JC013907, 2018.

Vereshchaka, A., Musaeva, E., and Lunina, A.: Biogeography of the Southern Ocean: environmental factors driving mesoplankton distribution south of Africa, PeerJ., 9, e11411, 10.7717/peerj.11411, 2021.

Weiss, J.: The dynamics of enstrophy transfer in two-dimensional hydrodynamics, Physica D., 48, 273–294, https://doi.org/10.1016/0167-2789(91)90088-Q, 1991.

~~Williams, G. D., Hindell, M., Houssais, M.-N., Tamura, T., and Field, I. C.: Upper ocean stratification and sea ice growth rates during the summer-fall transition, as revealed by Elephant seal foraging in the Adélie Depression, East Antarctica, Ocean Sci., 7, 185–202, https://doi.org/10.5194/os-7-185-2011, 2011.~~

Xia, X., Hong, Y., Du, Y., and Xiu, P.: Three types of Antarctic Intermediate Water revealed by a machine learning approach, Geophys. Res. Lett., 49, e2022GL099445, https://doi.org/10.1029/2022GL099445, 2022.

Zhang, Y., Chambers, D., and Liang, X.: Regional trends in Southern Ocean eddy kinetic energy, J. Geophys. Res. Oceans., 126, e2020JC016986, 10.1029/2020JC016973, 2021.

Zhu, G. P., Qian, H. R., Wei, L., Fach, B. A., Bestley, S., Yan, C. B., and Ashford, J. R.: Otolith chemistry indicates structuring of the Subantarctic myctophid Electrona carlsbergi in the Antarctic Circumpolar Current and Antarctic Slope Current off the South Shetland Islands, Palaeogeogr. Palaeoclimatol. Palaeoecol., 675, 113062, https://doi.org/10.1016/j.palaeo.2025.113062, 2025.